Harnessing unconventional buckling of tube origami metamaterials based on Kresling pattern

Emilio Turco [a], Emilio Barchiesi [a], Andrea Causin [a], Francesco dell'Isola [b], Margherita Solci [a]

[a] *Department of Architecture, Design and Urban planning (DADU), University of Sassari, Alghero (SS), Italy*
[b] *Department of Civil, Construction-Architectural and Environmental Engineering (DICEAA), University of L'Aquila, Italy*

A B S T R A C T

Kresling tube metamaterials are well known to exhibit a chirality-dependent exotic mechanical feature: a shortening or lengthening in the direction of the tube's axis produces a relative rotation of the two polygonal bases of the tube. This property can be easily grasped by fabricating a single-storey Kresling tube using cardboard. What has not been stressed much, if not even recognized, in the literature is the fact that such a mechanical feature is not depending only on the (chiral) geometrical pattern and unaffected by the in-plane/bending stiffness of facets and the creases' resistance to folding. Assuming to neglect the bending stiffness of facets, in the present contribution we prove, through some numerical simulations based on a discrete model taking into account inertial terms, that only when the in-plane-to-folding stiffness ratio is large the Kresling tube exhibits the aforementioned exotic feature as described in the literature. We also prove that a low in-plane-to-folding stiffness ratio reveals: *(i)* an unconventional buckling mode, both for axial shortening and lengthening, which resembles the mechanism of a camera diaphragm; *(ii)* a kind of auxetic behavior, *i.e.* a stenosis in a shortening test.

1. Introduction

The development of new materials is undoubtedly one of the most important challenges of this century, as the materials that are currently employed in engineering applications will soon be no more able to meet the most demanding needs coming from the industrial world. It is thus a necessity to develop new materials with improved properties, including mechanical ones, that can be otherwise regarded as outliers of Ashby diagrams. In this regard, it is relevant to note that, since recent achievements in production engineering have allowed for the precise control of the engineered micro-structure – *i.e.* how matter is arranged at a given sub-length-scale – of materials at the length scale of micrometer and nanometer, the way has been opened to the realization of newly (scientifically) designed materials, also called *metamaterials*. Such materials are designed so as to achieve exotic and/or extreme performances in terms of, among the others, acoustic and/or mechanical behaviors at length scales intervening in engineering applications.

The very nature of mechanical metamaterials consists in achieving mechanical properties that, at least qualitatively, do not depend on the constituent materials, but are arising from unit cells designed with sophisticated architectures, typically arranged in a periodic pattern (Kadic et al., 2019). It is therefore clear that, in the field of metamaterials, it is unavoidable to deal with, at least, two length scales, nothing hindering the fact that many more length scales, arranged into a hierarchy, could play a significant role in the mechanical behavior at large of a metamaterial. The need for distinguishing between these intervening length scales has brought to the utilization of the prefixes *macro* and *micro*. These prefixes, usually, do not refer to specific length scales. The prefix *macro* is indeed usually employed to identify the length scale at which the relevant, *i.e.* those due to its architecture, metamaterial properties are observed, normally that of the whole metamaterial specimen, whereas the prefix *micro* is employed to identify the length scale of the unit cells making up the metamaterial microstructure, which is determined during the design phase and is limited by the manufacturing process.

Many unit cell architectures have been investigated in the last twenty years, although mainly theoretically. As mentioned above, only recently the most promising architectures have been also experimentally tested. Macro-scale properties of interest in metamaterials

include negative Poisson's ratio – *i.e.* so-called auxetic behavior[1] – a low shear modulus, strong ultralight properties, large deformation regime, extreme damage tolerance, existence of solitary and/or shock waves, mechanical phase transition, axial-transverse-rotation coupling, acoustic/fracture cloaking, frequency band gaps, negative Poynting effect – possibly including its reversal – and many others, foldability/deployability or zero energy modes. Auxetic metamaterials, the adjective *auxetic*, originating from the Greek adjective *auxetikos*, include those metamaterials that, unlike most common materials, are characterized by the fact that, when subjected to a mono-axial tensile load, experience a size increase in the direction perpendicular to the loading one. Semi-auxetic materials are a special kind of auxetic materials, as they show such a transversal size increase only when subjected to loading in some directions, not all of them. The *synthesis problem* in metamaterials science basically reads as: given a desired (mechanical) behavior at large specified, as an instance, through some governing equations or material parameters, to find the micro-structure, if any, that realizes such a behavior. In a celebrated paper of theirs (Milton and Cherkaev, 1995), in 1995 Milton and Cherkaev were among the first who tried to give a relatively general answer to such a problem, proposing a rationale to produce metamaterials whose elastic properties are characterized by a desired elasticity tensor in the framework of Cauchy mechanics. In particular, they proposed penta-mode metamaterials, being characterized by the fact that five eigenvalues of the Voigt matrix representation of the elasticity tensor are very small with respect to the sixth one. Such a property can be equivalently stated by saying that the gradient of the placement field has a unit determinant, *i.e.* Jacobian. In Cauchy's theory of elasticity in small deformations, this implies a very large bulk modulus compared to the shear modulus and, consequently, Poisson's ratio is for these materials close to $\nu = 0.5$. It is thus possible to conclude that penta-mode metamaterials exhibit negligible shear effects, a typical feature of ideal incompressible fluids. In recent times, new classes of architectures, based on the deployable/foldable mechanisms, have gained attention in the realm of mechanical metamaterials, namely origami metamaterials, due to their complex mechanisms giving rise to extraordinarily exotic mechanical behaviors, and pantographic metamaterials, due to their unique deformation energy, which, at the leading order, follows a second-gradient energy pattern. A report on technological and scientific advancements in the field of metamaterials with pantographic motif is presented in Barchiesi et al. (2019), dell'Isola et al. (2019). While the initial goal in the realization of the first pantographic prototypes was the materialization of a lattice materials with predominant second gradient type behavior, many more recent investigations have found that these materials could have several applications.

Origami metamaterials take inspiration from the ancient Japanese art of folding sheets of paper for producing three-dimensional objects with a desired shape. In the 80s, Miura did put forward a proposal to create materials based on foldable unit cells, which was based on typical origami techniques (Miura, 1985). The main applications of such materials were at that time concerning solar panel packaging for space missions. As for the majority of metamaterials, the fine control in the fabrication allowed for by recent manufacturing techniques has made feasible their realization, that had been considered technologically infeasible for more than twenty years. As of today, several different structures have been proposed in the literature based on the periodic repetition in a two-dimensional array of a foldable unit cell, the geometrical problem of finding a transformation which is able to map a flat sheet into a folded one with desired shape being a crucial one in this field. The most common origami patterns the mechanical metamaterials literature is concerned with are based on the Miura and egg-box cells.

Here we shall be instead concerned with the so-called Kresling pattern. Introduced by Kresling in 1994 (Kresling, 1994), the homonymous (Kresling) pattern has been widely studied for its possible use in relevant real-world applications. Kresling pattern indeed confers extremely peculiar and interesting mechanical properties, the main one being the fact that Kresling tubes – henceforth also referred to as k-tubes – exhibit a strong coupling between axial displacement and twisting due to the chirality in three-dimensions of such a pattern (Hunt and Ario, 2005). Concerning possible applications of origami metamaterials based on the Kresling pattern, to start with, it is worth to mention that, very recently, studies (Forte et al., 2023) have proved that harnessing the chirality of Kresling tubes, and the consequent coupling between axial elongation/shortening and twisting, allows for realizing mechanical pixels. Other applications are related to mobility of robots in fluids, Ze et al. (2022), to the actual use of Kresling tubes for realizing robotic arms (Kaufmann et al., 2021; Kim and Cha, 2020), inflatable/collapsible structures (Chong et al., 2017) and biomedical applications (Kuribayashi et al., 2006). Finally, they are used as switches (Masana et al., 2020), the realization of force reducers (Yasuda et al., 2019), the realization of stiffeners (Al-Mansoori et al., 2020), besides being interesting for their (mechanical) phase transformation (Liu et al., 2021) and haptic (Chang et al., 2020) capabilities. Less specifically, applications can be found in the field of deployable structures, see Mis (2008), Miura (1985) and Vincent (2000) for applications concerning space missions and Georgakopolous et al. (2015) for application to antennas. It is also worth to mention the interesting capability possessed by the so-called one-stage Kresling tube, explored in Turco et al. (2023a) – basically a single-storey Kresling tube – to experience buckling while exhibiting a "closure" in a diaphragm-like way, which could be exploited in some technical applications. This capability, which depends on geometry and mechanical parameters, deserves in our opinion to be explored by means of a parametric analysis, also in the light of recent research in bistability of some origami metamaterials (Kamrava et al., 2017) and the sequential instability concept (Wheatcroft et al., 2023), that could lead to either the development of more complex exotic tunable buckling behaviors or the discovery of new properties of Kresling tubes. To this end, it would also be interesting to explore the mechanical behavior of a one-stage Kresling tube under various load conditions such forces which produce a shearing, bending and twisting.

Most likely, due to its microstructure, as the other origami metamaterials that have been studied from the continuum mechanics viewpoint, a two-dimensional continuum representation of Kresling tube metamaterials requires the use of generalized shell theory, while a one-dimensional continuum representation requires to resort to a Cosserat rod/beam. The evidences brought by investigations based on discrete simulations are useful to build and validate such generalized models. The last years have seen a renewed interest in generalized continua theories in the academic *milieu*. Such theories, that include second gradient ones, were introduced at the beginning of the twentieth century by the Cosserat brothers (Cosserat and Cosserat, 1896) and significantly developed in the early 1960s by Toupin (1964), Green et al. (1965), and Mindlin (1965), among the others. For a historical account of such theories, at least concerning the twentieth century, the reader is referred to the book by Maugin (2013). Clearly, said renewed interest is only for a small part due to the theoretical interest that generalized continua still have, because of some aspects that have yet to be elucidated completely. The main reason for such a renewed interest is the applications that generalized continua have in the field of mechanical metamaterials, in that they are capable of describing, as an instance,

[1] We stress that, actually, the stenosis in axial shortening occurs because the out-of-plane and in-plane symmetries have been broken in the discrete formulation of a cylinder that has been already compressed so as to obtain the Kresling pattern. In other words the volume is reduced in Kresling units in axial shortening due to the already twisted geometry – which promotes folding – and the low in-plane affine deformation stiffness, in the perspective of the minimum energy principle. The term *auxetic* has to be intended as an effective property since the base material is indeed not auxetic and the Kresling tube is not a solid material but rather a microstructured tube.

size effects, the existence of zero-energy modes, and effects due to non-local interactions, which cannot be taken into account for one reason or the other in classical first gradient, *i.e.* Cauchy, mechanics. In the last years generalized continua have been either employed or derived as mechanical models of microstructured media (dell'Isola et al., 2015, 2016; Alibert et al., 2003; Abdoul-Anziz and Seppecher, 2018). The identification, validation and formulation of generalized media has stimulated developments in several fields like discrete (Turco et al., 2016a,c,b; Turco and Rizzi, 2016; Turco et al., 2017, 2018) and semi-discrete (Andreaus et al., 2018) modeling making use of extensional and flexural elements (Steigmann and Faulkner, 1993; Cazzani et al., 2016a,b; Spagnuolo and Andreaus, 2018) along with its numerics, generalized shell theories (Altenbach and Eremeyev, 2009, 2013), mathematical foundations of second gradient continua (Eremeyev and Aifantis, 2017), and two-dimensional and three-dimensional finite elements with higher regularity (Abali et al., 2015; Niiranen et al., 2016; Khakalo and Niiranen, 2017; Balobanov et al., 2019). We remark that our main goal is to present phenomenological evidence by making use of a discrete model that could be used to formulate and validate a continuum model of Kresling metamaterial tubes. It is for this reason that we have tried our best to give a continuum perspective in view of a future homogenization. It is however to be mentioned that the model employed in our investigation is intrinsically discrete and has not been derived from a continuous one by discretization, except for the deformation energy associated to the in-plane affine motions of the facets, which has been derived consistently with a plane-stress continuous solid formulation. We also stress that the continuum model that we aim to get after homogenization is not a cylindrical tube before torsional buckling that, as correctly stated by the reviewer, contrarily to the discrete Kresling tube that has finite symmetry, has infinite symmetry. Indeed, the continuum model we refer to in the paper already has in its reference configuration a Kresling microstructure – encoded, as an instance, in its enriched kinematics and non-classical strain energy – that is that given by the buckling of a classical cylindrical tube.

Actually, the stenosis in axial shortening occurs because the out-of-plane and in-plane symmetries have been broken in the discrete formulation of a cylinder that has been already compressed so as to obtain the Kresling pattern. In other words, the volume is reduced in Kresling units in axial shortening due to the already twisted geometry – which promotes folding – and the low in-plane affine deformation stiffness, in the perspective of the minimum energy principle.

In order to try elucidating some issues mentioned in this introduction, aiming to shed light on what should be the kinematics of the target continuum model for Kresling origami metamaterials and what should be its properties at micro-scale to get desired macroscopic behaviors in terms of unconventional buckling behavior, in this paper we discuss a discrete model for Kresling tube metamaterials, Section 2, and a strategy to reconstruct its dynamical response, Section 3. Successively, in Section 4, we discuss some numerical simulations obtained using an in-house code based on the model and the numerical strategy discussed in the previous sections. Simulation results corroborate the claims made in the abstract and anticipate some concluding remarks, presented more extensively in Section 5, which lay the groundwork for future challenges.

2. Discrete element model of Kresling tubes

In this section we are going to present the model that has been employed in the present work to describe the mechanical behavior of the Kresling tube metamaterial. The model is a space-discrete one, it is namely a finite dimensional Lagrangian system. Accordingly, the model is completely characterized by the definition of the elementary contributions to the total kinetic and strain energies associated to each elastic element in the structure. Indeed, by assembling all such elementary contributions, one can write the action functional for the whole system. Hence, in this section, we will limit ourselves to describe the elementary kinetic and strain energy contributions, recalling what has been introduced more thoroughly in Turco et al. (2023b), which was developed purposely for origami-based metamaterials and gives details about the employed numerical solution method. It is worth to remark that an approach resembling the one developed in Turco et al. (2023b) had been previously proposed in the work (Liu and Paulino, 2017), but it was dealing only with static tests and was not worked out for origami-based metamaterials. Such an approach had been indeed originally developed, having as departure point traditional structural mechanics approaches, for pantographic structures (Turco et al., 2016a) and granular materials (Turco, 2018b; Turco et al., 2019). In this contribution we neglect the bending of facets. Indeed, since in the approach adopted in the present contribution two-dimensional bending elements consists of, at least, two adjacent triangles, the fact that facets in the Kresling pattern are triangles, along with the fact that no "fictitious triangles" are considered here in the framework of an "enhanced" description to further subdivide the facets, implies that bending of facets is not taken into account. It is worth remarking in this regard that a kind of "enhanced" description has been employed for the discrete modeling of beams in the context of pantographic fabrics, see Turco et al. (2018).

By referring to Fig. 1, which sketches a one-stage Kresling tube both in 3D view (a) and the corresponding folding pattern (b), we distinguish, besides nodes numbered using red color, facets, *i.e.* triangles constituting the origami, and panels, *i.e.* pair of facets sharing a side. Each one of the two origami components, facet and panel, is perfectly identified by the related nodes.

Let us refer again to the eth facet constituting the Kresling origami metamaterial. The vertices of the mid-plane of the eth facet, regarded as a prismatic body, will be denoted using the symbols i, j, and k. Such symbols stand for the node numbers associated to each vertex and take values in the discrete set of positive integers $[1; N_n]$, where the quantity N_n represents the total number of nodes. The coordinates of the vertices i, j, and k in the reference (undeformed) configuration, expressed in a global reference coordinate system, are collected in the vectors $\mathbf{X}_i$, $\mathbf{X}_j$, and $\mathbf{X}_k$, respectively, see Fig. 2. We assume as Lagrangian parameters to describe the motion the nodal displacements, therefore, the current position of the ith node, $\mathbf{x}_i$ can be written as $\mathbf{x}_i = \mathbf{X}_i + \mathbf{u}_i$ being $\mathbf{u}_i$ the displacement vector of the ith node.

2.1. Definition of the kinetic energy

We focus on the eth facet constituting the origami. The associated elementary contribution of the kinetic energy reads as

$$\mathcal{K}_e = \frac{1}{2}\int_{V_e} \rho\, \dot{\mathbf{u}}\cdot\dot{\mathbf{u}}\,\mathrm{d}V\,, \tag{1}$$

where the quantities ρ, V_e, and $\dot{\mathbf{u}}$ respectively stand for the spatial mass density, the three-dimensional domain the triangle is associated to – *i.e.* the extruded triangle – and the velocity of the elementary volume $\mathrm{d}V$. Considering a uniform mass density and thickness along facets, the use of a linear interpolation law for approximating the velocity in the prism gives for the elementary contribution of the eth facet

$$\mathcal{K}_e \approx \frac{1}{2}\int_{A_e} \rho\, s\,(\mathbf{B}_e\dot{\mathbf{u}}_e)\cdot(\mathbf{B}_e\dot{\mathbf{u}}_e)\,\mathrm{d}A = \frac{1}{2}\rho\, s\,\dot{\mathbf{u}}_e\cdot\left(\int_{A_e}\mathbf{B}_e^T\mathbf{B}_e\,\mathrm{d}A\right)\dot{\mathbf{u}}_e\,, \tag{2}$$

where A_e stands for the basis of the triangular prism and s is the thickness of the extruded triangle. The shape function matrix $\mathbf{B}_e$, along with the nodal velocity vector $\dot{\mathbf{u}}_e$, provides all what is needed to retrieve the approximation of the velocity vector in each point of the triangle, *i.e.* $\dot{\mathbf{u}} = \mathbf{B}_e\dot{\mathbf{u}}_e$. The shape function matrix $\mathbf{B}_e$ can be defined for any triangle by referring to a specific triangle (referred to in the sequel as the *reference* triangle) by virtue of the one-to-one correspondence between two any triangles. This is what we do in Eq. (4). The nodal

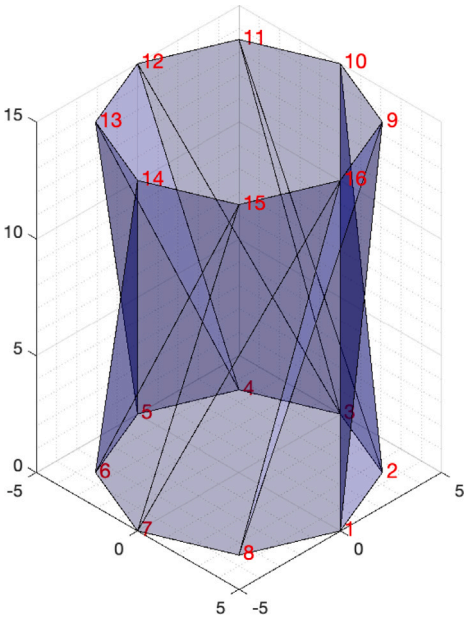

(a)

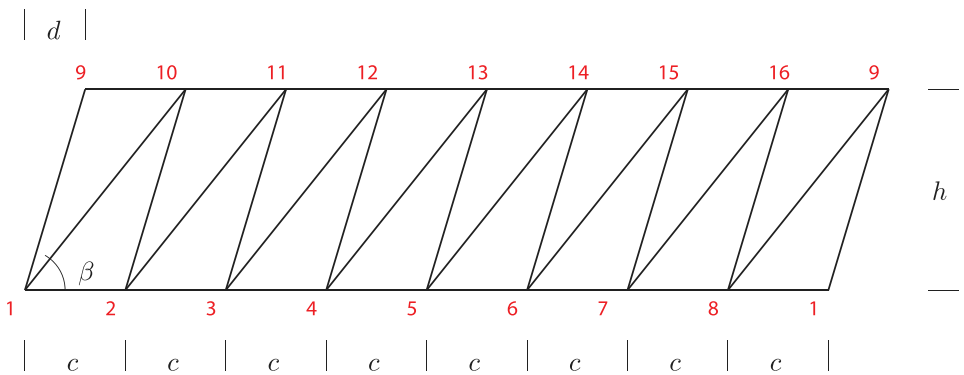

(b)

Fig. 1. One-stage Kresling tube: 3D view (a) and folding pattern (b).

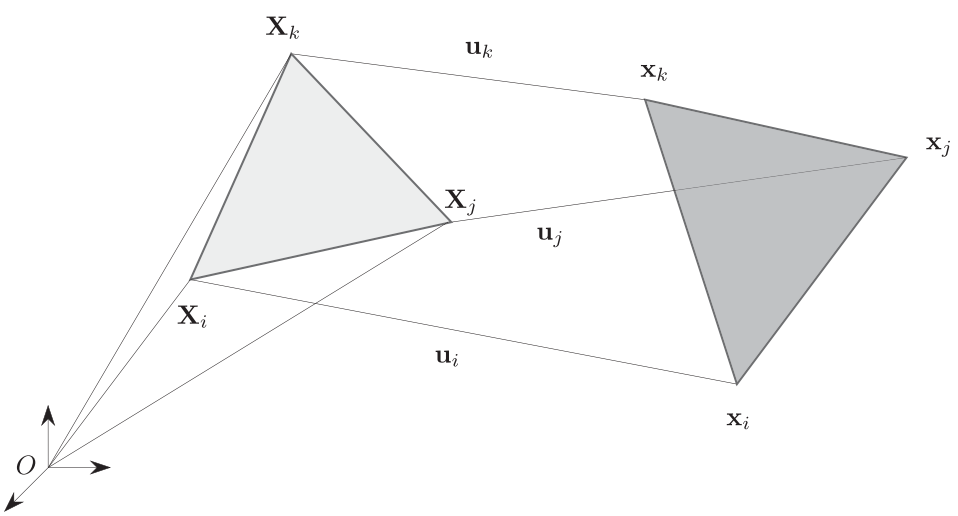

Fig. 2. Reference (white color) and current (light gray color) configurations for the affine deformation of a triangle.

velocity vector is obtained by collecting the velocities of the ith, jth and kth nodes

$$\dot{\mathbf{u}}_e = \begin{bmatrix} \dot{\mathbf{u}}_i \\ \dot{\mathbf{u}}_j \\ \dot{\mathbf{u}}_k \end{bmatrix}. \tag{3}$$

We now define the elementary contribution $\mathbf{M}_e$ of the considered eth prism to the mass matrix. As done before, we assume that the spatial mass density ρ is uniform. To get the sought elementary contribution it is now needed to evaluate the integral of $\mathbf{B}_e^T\mathbf{B}_e$ over the triangular basis of the prism. Since the evaluation of such an integral is easy when the integration domain coincides with the reference triangle whose vertices are the points with coordinates $(0,0)$, $(1,0)$ and $(0,1)$, we choose such a triangle as the reference triangle mentioned above. The shape function matrix $\widehat{\mathbf{B}}$ for the reference triangle can be written as

$$\widehat{\mathbf{B}} = \begin{bmatrix} (1-\xi-\eta) & 0 & 0 & \xi & 0 & 0 & \eta & 0 & 0 \\ 0 & (1-\xi-\eta) & 0 & 0 & \xi & 0 & 0 & \eta & 0 \\ 0 & 0 & (1-\xi-\eta) & 0 & 0 & \xi & 0 & 0 & \eta \end{bmatrix}, \tag{4}$$

where $0 \le \xi \le 1$, $0 \le \eta \le 1$ and $\xi + \eta \le 1$.

The above representation of the shape function matrix allows to write

$$\int_{A_e} \mathbf{B}_e^T\mathbf{B}_e \mathrm{d}A = 2A_e \int_{\widehat{A}} \widehat{\mathbf{B}}^T\widehat{\mathbf{B}}\mathrm{d}\widehat{A}, \tag{5}$$

with $\widehat{A}$ denoting the considered reference triangle and, at the same time, with an abuse of notation, also its area. Straightforward computations allow to write the element mass matrix for the eth triangle as

$$\mathbf{M}_e = \frac{\rho\, s\, A_e}{12}\begin{bmatrix} 2\mathbf{I}_3 & \mathbf{I}_3 & \mathbf{I}_3 \\ \mathbf{I}_3 & 2\mathbf{I}_3 & \mathbf{I}_3 \\ \mathbf{I}_3 & \mathbf{I}_3 & 2\mathbf{I}_3 \end{bmatrix}, \tag{6}$$

where the symbol $\mathbf{I}_3$ denotes the 3×3 identity matrix.

2.2. Definition of the in-plane deformation energy

At this point, we make the assumption that each facet, regarded as a prism, deforms affinely and in plane strain conditions, which means that strain is null along the thickness of the prism and uniform along each its triangular sections. Aimed at defining the strain energy of the generic facet, we make use of an idea which was originally introduced by Argyris et al. in the work (Argyris et al., 1997). Essentially, it relies on the observation that the deformation state of a triangular plate affinely deforming in its own plane can be retrieved by placing strain gauges at its sides, *i.e.* a strain gauges rosette[2] could be utilized.

This idea, together with the fact that the elastic energy of an isotropic, materially linear and geometrically nonlinear plate in plane strain conditions, undergoing an affine deformation, can be written as a quadratic form involving only squares of the strain (*i.e.*, changes of the sides' length), allows us to represent mechanically each facet through an equivalent determinate truss whose elements are the sides of the facets mid-plane.

To explain this work concretely, let us focus on what will be henceforth called the k-side, namely the side which lies in front of node k of the facet's mid-plane. The vectors $\mathrm{d}\mathbf{X}_k = \mathbf{X}_j - \mathbf{X}_i$ and $\mathrm{d}\mathbf{x}_k = \mathbf{x}_j - \mathbf{x}_i$, respectively, give the direction and length of the k-side. We define the Green's strain measure g_k of the k-side as given by the following expression

$$g_k = \frac{\ell_k^2 - L_k^2}{2L_k^2}, \tag{7}$$

with the squares of the current and the reference length of the k-side being denoted with $\ell_k^2 = \mathrm{d}\mathbf{x}_k \cdot \mathrm{d}\mathbf{x}_k$ and $L_k^2 = \mathrm{d}\mathbf{X}_k \cdot \mathrm{d}\mathbf{X}_k$, respectively. The positions of nodes i and j in the current configuration are given, respectively, by the formulas $\mathbf{x}_i = \mathbf{X}_i + \mathbf{u}_i$ and $\mathbf{x}_j = \mathbf{X}_j + \mathbf{u}_j$. These two last expressions constitute an indirect definition of nodal displacements, which have been adopted as the generalized coordinated of the finite dimensional Lagrangian system.

The stretching energy associated to the k-side is defined according to the following expression

$$S_k = \frac{1}{2} Y A_k L_k g_k^2, \tag{8}$$

where Y is the Young's modulus of the material the facet's mid-plane and A_k is the cross-sectional area of a fictitious rod placed along the k-side.

According to the fact that we represent mechanically each facet through an equivalent determinate truss whose elements are the sides of the facet's mid-plane, the sum of the stretching energies associated to each side of the considered triangle

$$S_e = S_i + S_j + S_k \tag{9}$$

equals the total strain energy stored in the eth prism and the areas of the fictitious rods placed along the sides of the facet's mid-plane A_i, A_j, and A_k can be indeed identified by equating the strain energy of the considered prism with the total stretching energy. The main ingredient of the identification between the facet and its equivalent truss is the link between the Green's strain measure associated to a considered facet's mid-plane side, say the i-side, and the (uniform, since we are in plane strain conditions and taken into account only affine deformations of the facet) Green–Saint-Venant strain tensor in three dimensions $\mathbf{G}$ associated to the eth facet

$$\ell_i^2 - L_i^2 = 2\mathrm{d}\mathbf{X}_i \cdot \mathbf{G}\mathrm{d}\mathbf{X}_i. \tag{10}$$

If we employ a three-dimensional local orthonormal reference system originating in the centroid of the facet's mid-plane and possessing two axes on such a mid-plane, the last relationship recasts as

$$\ell_i^2 - L_i^2 = 2\mathrm{d}\overline{\mathbf{X}}_i \cdot \overline{\mathbf{G}}\ \mathrm{d}\overline{\mathbf{X}}_i, \tag{11}$$

where vectors and tensors in such a local reference system are denoted using a superimposed bar. It is straightforward to note that, since we are considering plane strain conditions and only affine deformations of the facets, only the strain components $\overline{G}_{11}$, $\overline{G}_{22}$, and $\overline{G}_{12} = \overline{G}_{21}$, associated to the two orthonormal axes lying in the facet's mid-plane, are non-vanishing. Therefore, in order to get the components of the Green–Saint-Venant strain tensor associated to the eth facet in the local reference system, we want to solve the system of algebraic equations

$$\begin{aligned} \ell_i^2 - L_i^2 &= 2\mathrm{d}\overline{\mathbf{X}}_i \cdot \overline{\mathbf{G}}\ \mathrm{d}\overline{\mathbf{X}}_i, \\ \ell_j^2 - L_j^2 &= 2\mathrm{d}\overline{\mathbf{X}}_j \cdot \overline{\mathbf{G}}\ \mathrm{d}\overline{\mathbf{X}}_j, \\ \ell_k^2 - L_k^2 &= 2\mathrm{d}\overline{\mathbf{X}}_k \cdot \overline{\mathbf{G}}\ \mathrm{d}\overline{\mathbf{X}}_k. \end{aligned} \tag{12}$$

Essentially, the system above allows to retrieve the components $\overline{G}_{11}$, $\overline{G}_{22}$, and $\overline{G}_{12} = \overline{G}_{21}$ from the knowledge of the i-, j-, and k-side stretches. It is straightforward to see that the components of the Green–Saint-Venant strain tensor can be found as a linear combination of the stretches of the equivalent truss system. As mentioned above, we can identify the values of the cross-sectional areas of the fictitious rods making up the determinate truss system associated to the considered facet, and hence their stiffness a, by equating the total stretching energy associated to the sides of the considered facet's mid-plane, given by Eq. (9), and the energy associated to its in-plane deformation, that can be written as

$$E_e = \frac{1}{2} s A_e \mathbf{g} \cdot \mathbf{C}\mathbf{g}, \tag{13}$$

where the vector $\mathbf{g} = [\overline{G}_{11}\ \overline{G}_{22}\ 2\overline{G}_{12}]^T$ has been defined and where the quantities A_e and s stand for the area and the thickness of the

[2] A strain gauge rosette is a device able to detect the strain state in a point. In particular, it measures the strain along three fixed directions, therefore, it gives the strain tensor univocally.

considered triangle, respectively.[3] The matrix $\mathbf{C}$ represents in Voigt notation – in the local basis consisting of the two axes lying on the facet's mid-plane – the elasticity tensor associated to the material of the facet, which is assumed to obey Hooke's law. Such a matrix, assuming the material to be homogeneous and isotropic, and be the same for all the facets, for plane strain conditions reads as

$$\mathbf{C} = \frac{Y}{(1+\nu)(1-2\nu)} \begin{bmatrix} 1-\nu & \nu & 0 \\ \nu & 1-\nu & 0 \\ 0 & 0 & \frac{1-2\nu}{2} \end{bmatrix}, \tag{14}$$

where ν is the Poisson's ratio of the material and Y is, as defined above, the Young's modulus.

2.3. Folding energy

As briefly mentioned previously, bending of facets is here neglected. The only out-of-plane deformation energy consists of the strain energy associated to folding about a crease. We choose to approximate such an energy following a strategy outlined by Hencky in his celebrated doctoral thesis, see Hencky (1921). The original scope of Hencky was to estimate the buckling load of an Euler's beam. In the last decade, Hencky's idea has been exploited in several papers directed towards the modeling of pantographic structures (Turco et al., 2016a), beams (Turco, 2018a; Turco et al., 2022; Baroudi et al., 2019), and granular materials (Turco, 2018b; Turco et al., 2019; Turco, 2022).

Exploiting Hencky's idea means, in the present context, to deal with the folding of the origami metamaterial about a crease by connecting two adjacent facets – here called altogether a *panel* – through cylindrical hinges in such a way that only relative rotation around the crease is allowed and in placing a torsional spring, following Hooke's law, in-between the facets, so as to introduce an elastic resistance to such a relative rotation. The outcome of this approximation procedure is a lumped-parameter model.

The deformed configuration of a panel of an origami metamaterials is shown in Fig. 3, where m and n stand for the numbers associated to the facets of the panel. The vertices of the generic panel, *i.e.* the nodes of the constituting facets' mid-planes, have a label, namely i, j, k, and h, which take (different) integer values from 1 to the total number of nodes N_n. Each node in a panel places in the (undeformed) reference and current configurations and its position in these two configurations is denoted by $\mathbf{X}$ and $\mathbf{x}$, respectively, and labeled with the index associated to the node, namely i, j, k, or h for the generic panel. For the generic panel, we now define three orthonormal vectors, say $\{\mathbf{d}_1, \mathbf{d}_2, \mathbf{d}_3\}_m$, associated to the current configuration of the mth facet and three orthonormal vectors, say $\{\mathbf{d}_1, \mathbf{d}_2, \mathbf{d}_3\}_n$, associated to the current configuration of the nth facet, see Fig. 3. Referring to the mth facet – analogous considerations hold for the nth facet – the vector having 2 as subscript is parallel to the 1-side of the facet, that with subscript 3 is orthogonal to the plane containing the considered triangle and, finally, that with subscript 1 is such that $\mathbf{d}_{1m} = \mathbf{d}_{2m} \times \mathbf{d}_{3m}$. We denote with the symbol δ the dihedral angle between the planes containing the adjacent facets' mid-planes. Considering the reference configuration, an analogue definition can be made for both the two sets of orthonormal vectors associated to the facets of a panel and for the dihedral angle between two adjacent facets. In such a case, we use capital letters to indicate the orthonormal vectors, *i.e.* $\{\mathbf{D}_1, \mathbf{D}_2, \mathbf{D}_3\}_m$ for the mth facet and $\{\mathbf{D}_1, \mathbf{D}_2, \mathbf{D}_3\}_n$ for the nth facet. The dihedral angle in the reference configuration is denoted with δ_0.

[3] The surface of the eth facet's mid-plane can be computed via Heron's formula, employing only the lengths of the facet's mid-plane sides. By indicating with L_i, L_j and L_k the lengths of the sides that are opposite to the facet's mid-plane vertices i, j and k, respectively, the facet's mid-plane surface can be recovered using the expression $A_e = \sqrt{p(p-L_i)(p-L_j)(p-L_k)}$, where $p = \frac{1}{2}(L_i + L_j + L_k)$ is the semiperimeter.

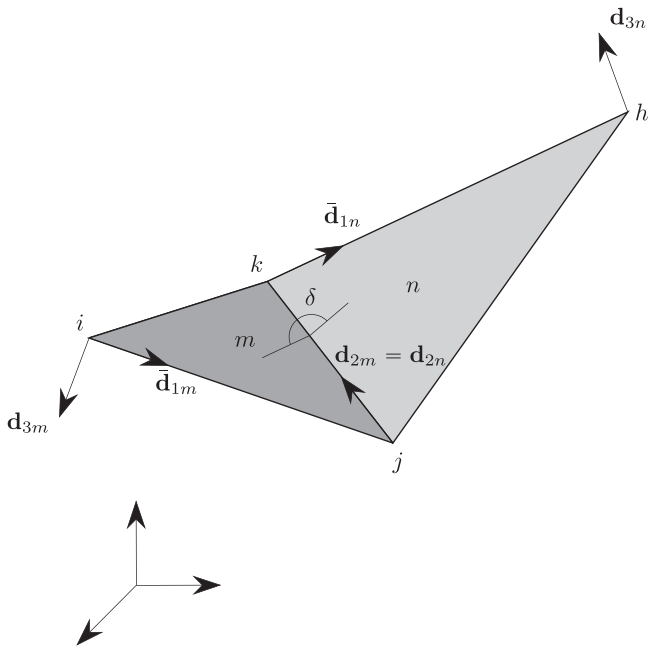

Fig. 3. Deformed configuration of a panel: nodes (i, j, k and h), facets (m and n) and panel along with the unit vectors ($\mathbf{d}_{3m}$, $\mathbf{d}_{3n}$) to compute the dihedral angle δ.

To sum up, the three orthonormal vectors associated to the current configuration of the mth and nth facets can be computed by means of the following formulas

$$\begin{aligned}
\bar{\mathbf{d}}_{1m} &= \frac{\mathbf{x}_j - \mathbf{x}_i}{\|\mathbf{x}_j - \mathbf{x}_i\|}, \\
\mathbf{d}_{2m} &= \frac{\mathbf{x}_k - \mathbf{x}_j}{\|\mathbf{x}_k - \mathbf{x}_j\|}, \\
\mathbf{d}_{3m} &= \frac{\mathbf{d}_{2m} \times \bar{\mathbf{d}}_{1m}}{\|\mathbf{d}_{2m} \times \bar{\mathbf{d}}_{1m}\|}, \\
\mathbf{d}_{1m} &= \mathbf{d}_{2m} \times \mathbf{d}_{3m}, \\
\bar{\mathbf{d}}_{1n} &= \frac{\mathbf{x}_h - \mathbf{x}_k}{\|\mathbf{x}_h - \mathbf{x}_k\|}, \\
\mathbf{d}_{2n} &= \mathbf{d}_{2m}, \\
\mathbf{d}_{3n} &= \bar{\mathbf{d}}_{1n} \times \mathbf{d}_{2n}, \\
\mathbf{d}_{1n} &= \mathbf{d}_{2n} \times \mathbf{d}_{3n}.
\end{aligned} \tag{15}$$

We shall now focus on the relative rotation of the two adjacent facets forming a panel with the aim of measuring folding of the origami metamaterial around creases. While the aforementioned relative rotation is clearly a suitable ingredient for building such a measure, it still needs to be worked out. Before attempting at getting a real quantity from such a relative rotation, we note that the local bases $\{\mathbf{d}_{1m}, \mathbf{d}_{2m}, \mathbf{d}_{3m}\}$ and $\{\mathbf{d}_{1n}, \mathbf{d}_{2n}, \mathbf{d}_{3n}\}$ are constructed making use of a (possibly stretched) side of the deformed mth and nth facet's mid-plane, respectively. Therefore, the transformation that leads from $\{\mathbf{d}_{1m}, \mathbf{d}_{2m}, \mathbf{d}_{3m}\}$ to $\{\mathbf{d}_{1n}, \mathbf{d}_{2n}, \mathbf{d}_{3n}\}$, while being a rotation, is not occurring around the side shared by the mid-planes of the facets m and n, which is what we are interested in. In other words, such a transformation is obtained as the composition of a rotation around the crease of the panel and a spurious rotation induced by the in-plane affine deformation of the mth and nth facets' mid-planes. In order to filter out such a spurious rotation we exploit the right polar decomposition of the tensor $\mathbf{F}$ associated to the deformation in a three-dimensional space of the mth and nth facets.

It is easy to see that the deformation gradient tensor $\mathbf{F}_m$ for the mth facet fulfills the following relationships (analogous relationships hold

for $\mathbf{F}_n$.)

$$\begin{aligned}\mathbf{F}_m(\mathbf{X}_j-\mathbf{X}_i)&=\mathbf{x}_j-\mathbf{x}_i\\ \mathbf{F}_m(\mathbf{X}_k-\mathbf{X}_j)&=\mathbf{x}_k-\mathbf{x}_j\\ \mathbf{F}_m\mathbf{D}_{3m}&=\mathbf{d}_{3m}\,.\end{aligned}\tag{16}$$

The previous relationships constitute a system of nine linearly independent algebraic equations in the nine independent components of $\mathbf{F}_m$. We note that, as long as the mth triangle does not collapse into a point, such a system admits a unique solution, which can be computed through elementary algebraic manipulations.

We recall that the right polar decomposition formula, that we intend to apply to the deformation gradient tensors associated to the mth and nth triangles, reads as

$$\mathbf{F}=\mathbf{R}\mathbf{U}\,,\tag{17}$$

where $\mathbf{R}$ is a proper orthogonal tensor representing the rotational part of $\mathbf{F}$ and $\mathbf{U}$ is a positive definite symmetric tensor representing the stretch part of $\mathbf{F}$. It is well known that, since

$$\mathbf{F}^T\mathbf{F}=\mathbf{U}^T\mathbf{R}^T\mathbf{R}\mathbf{U}=\mathbf{U}^T\mathbf{U}=\mathbf{U}^2\,,\tag{18}$$

the second order tensor $\mathbf{U}^2$ is positive definite and symmetric. Because of these properties, it is meaningful to consider its square root, namely $\mathbf{U}=\sqrt{\mathbf{F}^T\mathbf{F}}$, that can be computed by means of its spectral decomposition, *i.e.*

$$\sqrt{\mathbf{F}^T\mathbf{F}}=\mathbf{V}\sqrt{\mathbf{\Lambda}}\mathbf{V}^T\,,\tag{19}$$

where the quantity $\mathbf{V}$ is the orthogonal matrix that collects the eigenvectors of the symmetric tensor $\mathbf{F}^T\mathbf{F}$ and the quantity $\mathbf{\Lambda}$ is the diagonal matrix whose elements are the eigenvalues of $\mathbf{F}^T\mathbf{F}$ arranged in the same order as that of the corresponding eigenvectors in the matrix $\mathbf{V}$. Making use of the right polar decomposition formula (17), when $\mathbf{U}$ is known we can compute the rotation matrix $\mathbf{R}$ as $\mathbf{R}=\mathbf{F}\mathbf{U}^{-1}$. Let be $\mathbf{R}_m$ and $\mathbf{R}_n$ rotational parts of the deformation gradients of the mth and nth facet, respectively. Then, the finite relative rotation tensor $\Delta\mathbf{R}$ of the mth and nth facets, occurring around the crease, can be defined as

$$\Delta\mathbf{R}=\mathbf{R}_m^T\mathbf{R}_n\,.\tag{20}$$

The Rodrigues' formula can be used to express in a more insightful way a rotation tensor $\mathbf{R}$

$$\mathbf{R}=\cos\varphi\mathbf{I}+(1-\cos\varphi)\mathbf{e}\otimes\mathbf{e}+\sin\varphi\mathbf{E}\,,\tag{21}$$

being $\mathbf{e}$ the rotation axis, φ the rotation's signed amplitude, and $\mathbf{E}$ the tensor whose axial vector is $\mathbf{e}$, namely the tensor such that $\mathbf{E}\mathbf{v}=\mathbf{e}\times\mathbf{v}$ for any vector $\mathbf{v}$. Using Eq. (21), we can prove that

$$2\cos\varphi=\mathrm{tr}(\mathbf{R})-1\,,\quad 2\sin\varphi\,\mathbf{e}=\mathbf{R}_\times\,,\tag{22}$$

where $\mathrm{tr}(\cdot)$ stands for the trace of a matrix and $\mathbf{R}_\times$ is the axial vector of the skew symmetric part of $\mathbf{R}$. Defining the rotation axis as

$$\boldsymbol{\vartheta}=2\tan\left(\frac{\varphi}{2}\right)\mathbf{e}\,,\tag{23}$$

we can rewrite the Rodrigues' formula as

$$\mathbf{R}=\frac{1}{4+\vartheta^2}\left((4-\vartheta^2)\mathbf{I}+2\,\boldsymbol{\vartheta}\otimes\boldsymbol{\vartheta}+4\mathbf{E}_{\boldsymbol{\vartheta}}\right)\,,\tag{24}$$

being $\vartheta^2=\boldsymbol{\vartheta}\cdot\boldsymbol{\vartheta}$ the norm of the chosen rotation axis and $\mathbf{E}_{\boldsymbol{\vartheta}}\mathbf{v}=\boldsymbol{\vartheta}\times\mathbf{v}$ the tensor whose axial vector is the chosen rotation axis. Note that, since the finite relative rotation tensor $\Delta\mathbf{R}$ is orthogonal, by using (22) and the half-angle trigonometric formula, we can write the relative finite rotation vector as

$$\Delta\boldsymbol{\vartheta}=\frac{2(\Delta\mathbf{R})_\times}{1+\mathrm{tr}(\Delta\mathbf{R})}\,.\tag{25}$$

At this point, all is set to finally define the folding strain energy for the pth panel. Such an energy, taking inspiration from the impenetrability constraint introduced in Tran et al. (2021), Tran and Barchiesi (2022) in the context of a discrete model for brick masonry structures, aimed at taking into account the contact between two adjacent facets, reads as

$$\begin{aligned}E_l&=l_1+\frac{l_2}{\delta-\bar\delta_l}\,,\qquad \bar\delta_l<\delta<\delta_l^*\,,\\ E_q&=\frac{1}{2}b\|\mathbf{X}_k-\mathbf{X}_j\|(\delta-\delta_0)^2\,,\qquad \delta_l^*<\delta<\delta_r^*\,,\\ E_r&=r_1+\frac{r_2}{\bar\delta_r-\delta}\,,\qquad \delta_r^*<\delta<\bar\delta_r\,,\end{aligned}\tag{26}$$

where the quantity b is a stiffness per unit length, the quantity δ is the approximated expression of the dihedral angle,

$$\delta=2\arctan\frac{\|\Delta\boldsymbol{\vartheta}\|}{2}\,,\tag{27}$$

and $\bar\delta_l$ and $\bar\delta_r$ are the values of the dihedral angle corresponding to the left and the right potential walls, respectively. In our case, we have $\bar\delta_l=0$ and $\bar\delta_r=2\pi$. The parameters l_1, l_2, δ_l^*, r_1, r_2, and δ_r^* need to be evaluated so as to fulfill the continuity of the strain energy function along with that of its first and second derivatives. Indeed, we remark that, in our strategy to reconstruct the dynamical equilibrium path, we necessitate both of the strain energy's first derivative, *i.e.* the structural response, and of the strain energy's second derivative, *i.e.* the tangent stiffness matrix. The sought parameters read as

$$\begin{aligned}\delta_l^*&=\frac{2}{3}\left(\delta_0+\frac{\bar\delta_l}{2}\right)\,,\\ l_2&=-b\|\mathbf{X}_k-\mathbf{X}_j\|(\delta_l^*-\delta_0)(\bar\delta_l-\delta_l^*)^2\,,\\ l_1&=\frac{1}{2}b\|\mathbf{X}_k-\mathbf{X}_j\|(\delta_l^*-\delta_0)^2-\frac{l_2}{\bar\delta_l-\delta_l^*}\,,\\ \delta_r^*&=\frac{2}{3}\left(\delta_0+\frac{\bar\delta_r}{2}\right)\,,\\ r_2&=b\|\mathbf{X}_k-\mathbf{X}_j\|(\delta_r^*-\delta_0)(\bar\delta_r-\delta_r^*)^2\,,\\ r_1&=\frac{1}{2}b\|\mathbf{X}_k-\mathbf{X}_j\|(\delta_r^*-\delta_0)^2-\frac{r_2}{\bar\delta_r-\delta_r^*}\,.\end{aligned}\tag{28}$$

Fig. 4 shows the plots the strain energy defined by (26) against the quantity δ for $\delta_0=\pi/2$ (on the left), $\delta_0=\pi$ (in the middle) and $\delta_0=3\pi/2$ (on the right). Remark that the quantity δ in the formulas above is not the dihedral angle, but it is rather an equivalent approximated quantity. Indeed, we have $\delta=\|\boldsymbol{\vartheta}\|=2\tan\frac{\varphi}{2}$. However, this quantity tends to the dihedral angle when this last is small. In each of the plots in Fig. 4 the left and right sub-interval inverse proportionality laws in (26), along with the vertical lines corresponding to δ_l^* and δ_l^*, are reported in dark yellow and dark orange colors, respectively.

3. Stepwise analysis strategy for getting time-evolution response of Kresling tubes

While in Section 2 we have described the adopted modeling strategy, we now address the numerical strategy needed to reconstruct the whole equilibrium path of the discrete system under consideration. Even if in this paper we are interested in analyzing one-stage Kresling tubes, that described below is a general strategy adaptable to any discrete, or discretized, mechanical system. It is essentially based on an original work of Casciaro (1975) and the successive paper (Turco, 2021), where the whole procedure is reviewed and more detailed explanation of the used formulas is provided along with some comments aimed at shedding light on some unaddressed issues. However, the strategy proposed here differs from the original work of Casciaro for two reasons: *(i)* it uses as primary variables displacements instead of velocities, see Turco et al. (2023a); *(ii)* it is adapted for mechanical problems where the external world acts onto the system only by prescribing evolution laws for the displacement of a set of nodes.[4]

[4] It is an empirical observation that for systems with high-frequency vibrations the accuracy of velocities computed on the basis of interpolated

At first, we specify that the presented time-integration scheme is based on the subdivision of the time horizon of the simulation in N time steps of equal length Δt.[5] Assuming as known the initial conditions, *i.e.* the initial displacement and velocity vectors $\mathbf{u}_0 = \mathbf{u}(t = 0)$ and $\dot{\mathbf{u}}_0 = \dot{\mathbf{u}}(t = 0)$, respectively, we want to compute, sequentially, the solution at times $t_{j+1} = t_j + \Delta t$ $(j = 0, 1, \dots, N)$. Clearly, the basic brick to build a sequential solution process consists of being able to solve the following problem: assuming as known the solution for t_j, *i.e.* we know the vectors $\mathbf{u}_j = \mathbf{u}(t_j)$ and $\dot{\mathbf{u}}_j = \dot{\mathbf{u}}(t_j)$, how do we compute the solution $\mathbf{u}_{j+1}$ and $\dot{\mathbf{u}}_{j+1}$?

To start answering to the last question, we note that Casciaro's scheme is based on the discrete form of the momentum-impulse relationship which, using already defined symbols, can be written as

$$\mathbf{M}(\dot{\mathbf{u}}_{j+1} - \dot{\mathbf{u}}_j) + \left(\left(\frac{1}{2} - \alpha\right)(\mathbf{s}_j - \mathbf{f}_j) + \left(\frac{1}{2} + \alpha\right)(\mathbf{s}_{j+1} - \mathbf{f}_{j+1})\right)\Delta t = \mathbf{0}\,, \quad (29)$$

where the first term can be interpreted as a finite-difference approximation of the momentum rate, while the second term is the average net impulse. This last term is obtained by means of two dimensionless weighting factors depending upon the parameter α, which will be defined and suitably chosen below.Since for each time step we are considering as unknowns the vectors $\mathbf{u}_{j+1}$ and $\dot{\mathbf{u}}_{j+1}$, an additional set of equations is necessary to equate the number of independent equations and that of the unknowns. This set is found by choosing as interpolation law for the displacement vector a quadratic rule

$$\mathbf{u}_{j+1} = \mathbf{u}_j + \left(\left(\frac{1}{2} - \beta\right)\dot{\mathbf{u}}_j + \left(\frac{1}{2} + \beta\right)\dot{\mathbf{u}}_{j+1}\right)\Delta t\,. \quad (30)$$

We note that the parameters used to express the interpolation rule above are the displacement and the velocity vectors at the beginning of the time step and the velocity vector at the end of the time step. In other words, the quadratic rule, besides the displacement at the beginning of the time step, makes use of velocities, namely the time derivative of the displacement, at the beginning and at the end of the time step. Readers who usually work with B-splines (Aristodemo, 1985; Greco and Cuomo, 2013) and NURBS (Non Uniform Rational Basis Splines) (Cazzani et al., 2016a) should be familiar with this idea. It has to be remarked that, as for the discrete form of the momentum-impulse relationship above, also in this case a dimensionless parameter, called β, is used, which is characteristic of the Casciaro's integration scheme and weights the velocity at the beginning and that at the end of the time step.

To sum up, Casciaro's scheme makes use of the momentum-impulse relationship and a quadratic B-spline interpolation for the displacements. Two dimensionless parameters α and β are introduced in the integration scheme that, when finely tuned, optimize the performances of the scheme. Following Casciaro's idea, these two dimensionless parameters have to be tuned according to the estimate of the first, T_1, and of the last, T_N, natural periods of the Lagrangian system under consideration and the selected time-step length Δt that, usually, must be in turn chosen on the basis of the problem to tackle (usually the loading law and the first natural period). Hence, an eigenvalue analysis, limited to the first and the last natural periods computed in the reference configuration, has to be performed. This preliminary analysis involves the mass matrix $\mathbf{M}$ and the stiffness matrix $\mathbf{K}$ computed in the reference configuration, *i.e.* $\mathbf{K}(\mathbf{u} = \mathbf{0})$.

The rule proposed in Casciaro's work (Casciaro, 1975) for choosing in an *optimal* way the two dimensionless weighting parameters α and β is based on the analysis of a one-degree-of-freedom system in linear regime. The main idea is to adapt the dimensionless weighting parameters to the chosen time-step length, which generally is suggested by the

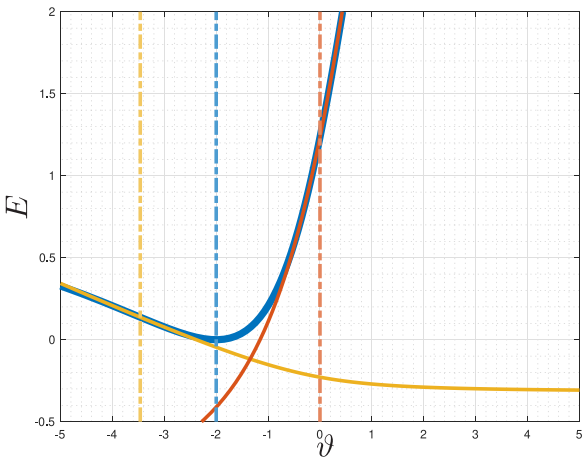

(a) $\delta_0 = \dfrac{\pi}{2}$

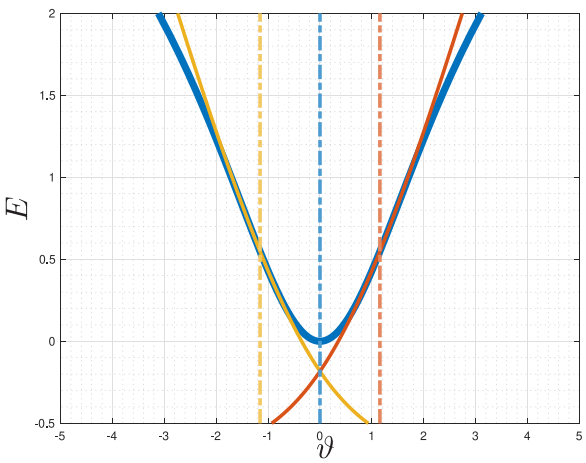

(b) $\delta_0 = \pi$

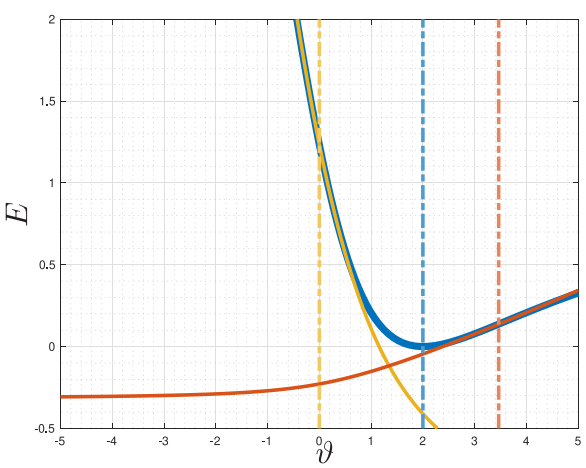

(c) $\delta_0 = \dfrac{3\pi}{2}$

Fig. 4. Folding strain energy E for $\delta_0 = \pi/2$ (a), $\delta_0 = \pi$ (b), and $\delta_0 = 3\pi/2$ (c): quadratic law in blue color, left inverse law in dark yellow and right inverse law in dark orange.

displacements is less than that achieved when interpolating directly the velocities, thus the introduced modification allows to get an algorithm that is significantly more stable.

[5] This hypothesis is not essential and can be easily removed if necessary.

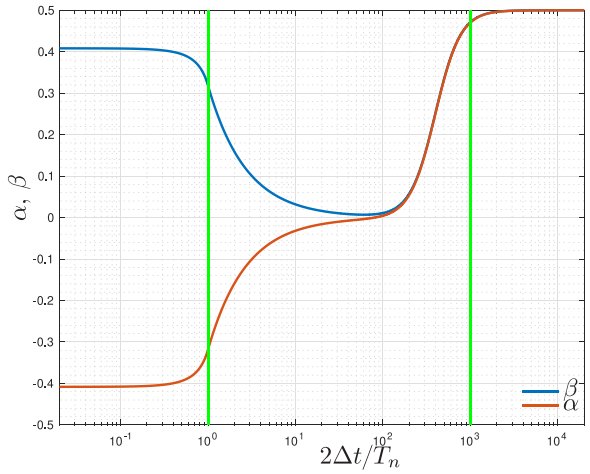

Fig. 5. Optimal parameters α and β *vs.* dimensionless time-step length $2\Delta t/T_n$ (vertical green lines indicate T_n, on the left, and T_1, on the right).

problem: *(i)* natural periods generally well represent the system under consideration; *(ii)* loading is usually described as a linear piece-wise function of time, therefore the time-step interval has to be chosen in order to well-represent the loading process; *(iii)* the available computing resources are always limited, hence too small time-step intervals are impracticable; *(iv)* accuracy of modern computers is nowadays large but not infinite and, as a consequence, problems as numerical drift or instability deriving from round-off errors have to be expected.

Following Casciaro, optimal values of the dimensionless parameters α and β can be found according to the following formulas

$$\begin{aligned} \beta = -\alpha &= \sqrt{-\frac{1}{4}+\frac{1}{\gamma^2}-\frac{1+\sqrt{1+\tan^2\gamma}}{2\tan^2\gamma}}\,, \qquad 0<\gamma<\frac{\pi}{2}\,, \\ \beta = -\alpha &= \sqrt{-\frac{1}{4}+\frac{1}{\gamma^2}-\frac{1-\sqrt{1+\tan^2\gamma}}{2\tan^2\gamma}}\,, \qquad \frac{\pi}{2}<\gamma<\pi\,, \end{aligned} \tag{31}$$

having introduced the dimensionless parameter $\gamma = 2\pi\Delta t/T_n$. We observe that Eq. (31), when $\Delta t \to 0$, gives $\beta = -\alpha = 1/\sqrt{6}$. Differently, when $\Delta t \to T_n/2$, the expression $\beta = -\alpha = 1/\pi$ is obtained.

In the case $\Delta t > T_n/2$, optimal values of the dimensionless parameters have the expression

$$\alpha = -\frac{T_n}{2\pi\Delta t}+\frac{c^3}{1+2c^3}\,, \quad \beta = \frac{T_n}{2\pi\Delta t}+\frac{c^3}{1+2c^3}\,, \quad c = \frac{2\Delta t - T_n}{T_1 - T_n}\,. \tag{32}$$

Formulas (32) contain both a hyperbola branch – which links the optimal values of α and β at the end of the interval $\Delta t < T_n/2$ – and the ratio between two cubic polynomials, which tends – when $\Delta t \to \infty$ – to the value 1/2. As a consequence, the corresponding values of α and β are capable to reproduce a quasi-static solution. Formulas (31) and (32) are synthesized in the plot reported in Fig. 5. Finally, we bring to the attention of the reader that, when a nonlinear problems have to be tackled, small values of the time-step length have to be used anyway.

Having sketched the time integration scheme that we intend to use, we shall outline the solution strategy to tackle the nonlinear problem to be solved. Roughly speaking, we have, using Casciaro's scheme, a way to solve a sequence of initial problems. Still, for each such initial problem, we have to solve a nonlinear problem. The key tool of the solution strategy for the nonlinear problem is the first order Taylor expansion of the structural reaction $\mathbf{s}_{j+1} = \mathbf{s}(\mathbf{u}_{j+1})$, which can be written as

$$\mathbf{s}_{j+1} \approx \mathbf{s}_j + \mathbf{K}_j(\mathbf{u}_{j+1} - \mathbf{u}_j)\,, \tag{33}$$

where $\mathbf{K}_j$ is the stiffness matrix computed at the beginning of the considered time interval:

$$\mathbf{K}_j = \left.\frac{\mathrm{d}\mathbf{s}}{\mathrm{d}\mathbf{u}}\right|_{\mathbf{u}_j}\,. \tag{34}$$

Since the velocity variables collected in the vector $\dot{\mathbf{u}}_{j+1}$ can be eliminated, by using Eqs. (30), from the system formed by Eq. (29) and (30), it is found that Eqs. (30)–(29), together with the Taylor expansion (33), are the strictly necessary tools to apply a Newton-like algorithm for the considered problem. From the formula expressing the reminder computed at the ith iteration

$$\mathbf{r}_i = \mathbf{M}(\dot{\mathbf{u}}_{j+1,i} - \dot{\mathbf{u}}_j) + \left(\left(\frac{1}{2}-\alpha\right)(\mathbf{s}_j - \mathbf{f}_j) + \left(\frac{1}{2}+\alpha\right)(\mathbf{s}_{j+1,i} - \mathbf{f}_{j+1})\right)\Delta t\,, \tag{35}$$

the solution estimate is updated, following a Newton-like strategy, through the recurrent formula

$$\mathbf{u}_{j+1,i+1} = \mathbf{u}_{j+1,i} - \mathbf{H}_j^{-1}\mathbf{r}_j\,, \tag{36}$$

where we employ the iteration matrix $\mathbf{H}_j$ that is defined as

$$\mathbf{H}_j = \nabla\mathbf{r}|_j = \frac{1}{\frac{1}{2}+\beta}\mathbf{M} + \left(\frac{1}{2}+\alpha\right)\mathbf{K}_{j,i}\,. \tag{37}$$

The equation above makes opportune noting that, by considering inertial forces, we can avoid the well-known multi-bifurcation problem occurring in the static analysis of Kresling-tube metamaterials subjected to axial compression forces, and hence find a numerically stable equilibrium solution for large deformations.

The algorithm sketched in the foregoing is more adapt for addressing the solution of problems involving origami metamaterials, modeled as explained in the previous sections, compared to the original scheme proposed by Casciaro. A slight modification of Casciaro's scheme, using as primary variable the displacement vector instead of the velocity one, does not change significantly the properties of the scheme but, in practice, it allows to get an algorithm that is significantly more stable.

Before reporting the numerical simulations obtained by using the algorithm described above, it is worth remarking that, even for dynamic problems that are more complex than those addressed in this contribution, the use of the Newton method does not suffer the limitations that it usually experiences for static problems. Indeed, as it is well documented in the literature, when static problems are tackled, Newton's method is not able to manage limit points, *i.e.* configurations that make singular the stiffness matrix $\mathbf{K}$. This is because such a method uses as iteration matrix the tangent stiffness matrix. As a consequence, its use for the static analysis of systems exhibiting limit points is not advisable. Conversely, when dynamic analyses are considered, since the iteration matrix also includes an additive contribution containing the mass matrix (which is always different from zero), see (37), then making use of the Newton scheme is always possible.

Finally, before to show and discuss the results of a selected number of numerical simulations, we precise that the model presented in Section 2 and the numerical strategy depicted in Section 3 were implemented in a Matlab code developed in-house.

4. Numerical simulations

In this section we present and discuss some numerical simulations with the objective of exploring the mechanical behavior of one-stage Kresling tubes. In particular, we discuss two cases: the shortening and the lengthening of a one-stage Kresling tube, having a fixed geometry, when varying the ratio between the stiffness a – of each element of the equivalent determinate truss system that models the in-plane deformation behavior of facets constituting the origami tube – and the stiffness b of the torsional springs modeling the folding rigidity of two facets sharing a side. All the numerical data provided in this section are expressed in the MKS system of units.

Specifically, we consider the one-stage Kresling tube reported in Fig. 1, which is based on two regular octagons, *i.e.* the bottom and top bases of the tube are regular octagons. The geometrical parameters characterizing the one-stage Kresling tube are the side length c, the height h and the gap d, see Fig. 1(b). For the numerical simulation described below, we assume $c = 3.8268$, $h = 15$ and $d = 3.8268$.[6]

[6] The chosen geometry has an angle β approximately equal to 71.6°.

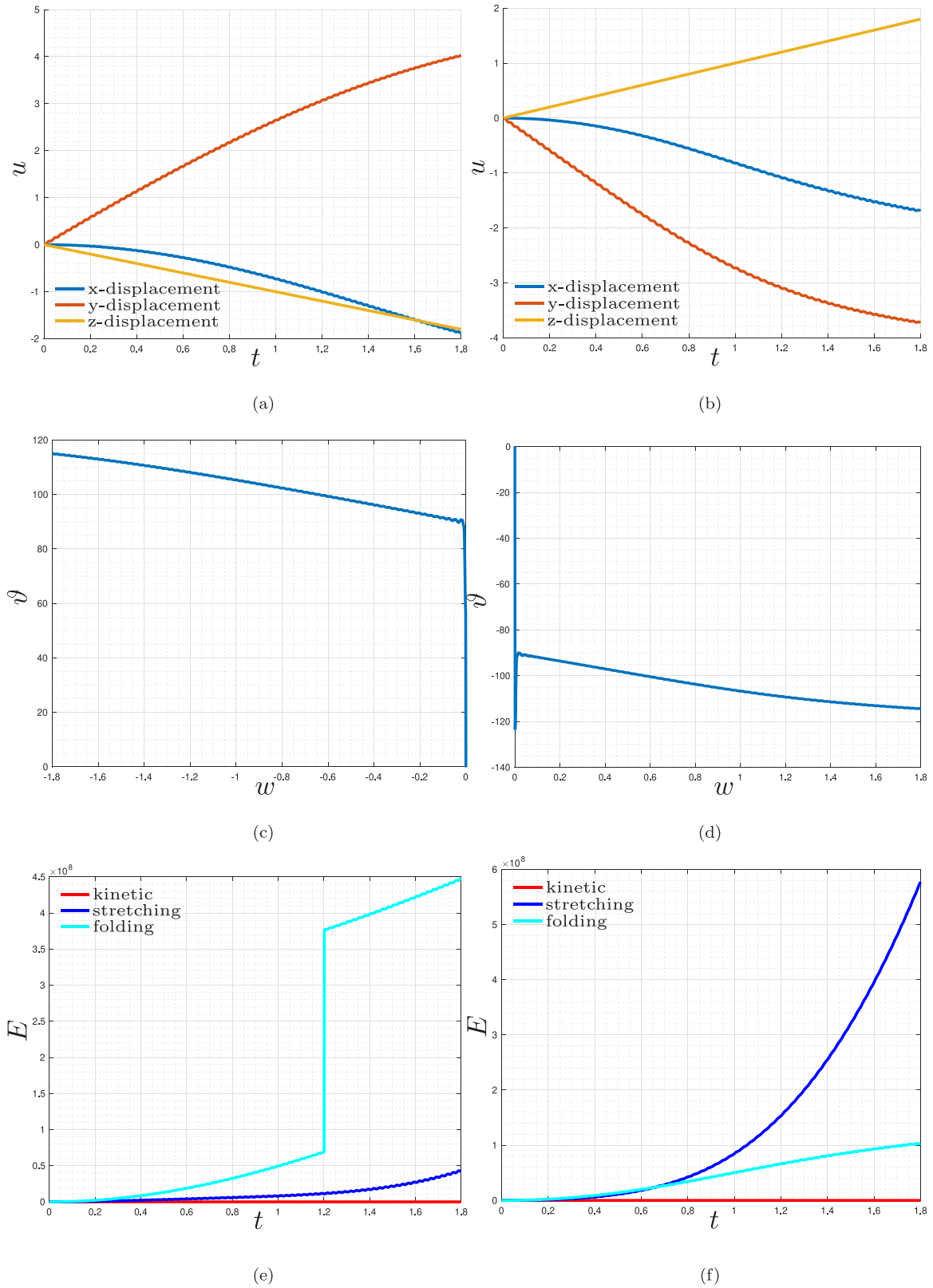

Fig. 6. Shortening (on the left) and lengthening (on the right) of the one-stage Kresling tube for $a/b = 1000$: time evolution of the displacement of the 9th node (a)–(b), rotation of the tube's top base *vs.* assigned vertical displacement (c)–(d) and time evolution of energies – kinetic, stretching and folding – (e)–(f).

In what follows, we report the results of two shortening and two lengthening tests performed by varying the ratio a/b. Specifically, for each shortening/lengthening test we consider two case studies: in the first case study the stiffness ratio is equal to $a/b = 1000$, while in the second case study the stiffness ratio is equal to $a/b = 0.1$. The stiffness ratio is changed by varying the value of the stiffness a only, while the stiffness b is always assumed to be equal to $b = 10^6$. We note that the first case describes a Kresling tube with a stretching stiffness that is

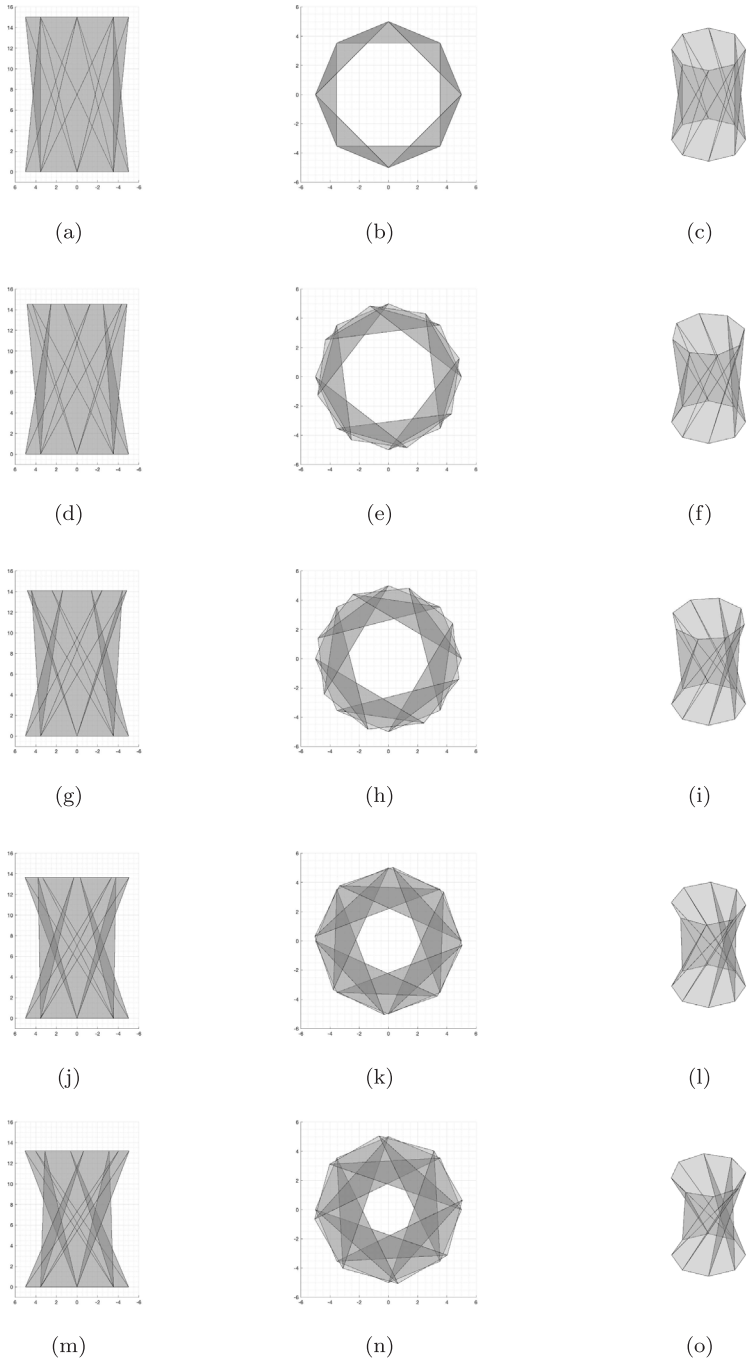

Fig. 7. Stroboscopic shoots for the shortening test of the one-stage Kresling tube for $a/b = 1000$: side (on the left), top (on the middle) and 3D (on the right) views for $t/t_o = 0$ (first row), $t/t_o = 0.25$ (2nd row), $t/t_o = 0.5$ (3rd row), $t/t_o = 0.75$ (4th row) and $t/t_o = 1$ (5th row).

very large with respect to the folding stiffness. Therefore, such a case well represents the usual origami's made up of folded paper sheets. The second ratio that has been considered can be instead associated with an origami metamaterial realized either by reinforcing the creases and/or by employing an extremely deformable material for facets, possibly a metamaterial by itself. This features are not unamenable to today's additive manufacturing techniques. Having fixed the geometry and using the data described above, we shall introduce the conditions on nodes. The nodes at the bottom base of the tube have been completely fixed, *i.e.* no displacement is allowed. Differently, the nodes at the top base of the tube are free to move in the plane identified by the bases of the tube, while their displacement along the tube's axis follows an assigned displacement time law that is the same for all the nodes. The displacement time law that has been chosen is linear, starting from zero and having constant (loading) rate $\bar{v}$. Finally, we assume $\rho = 100$ and $s = 0.1$ for the mass density and the thickness of the facets constituting the Kresling tube, respectively.

4.1. Shortening and lengthening tests for $a/b = 1000$

We here consider shortening and lengthening tests for the case study characterized by $a/b = 1000$. Preliminarily, we perform a modal analysis in correspondence of the reference configuration to compute the first T_1 and the last T_n natural periods, as needed to calibrate the parameters utilized by the employed Casciaro's integration scheme. For the considered case, we have $T_1 = 0.0325$ and $T_n = 0.00221$. Selecting as

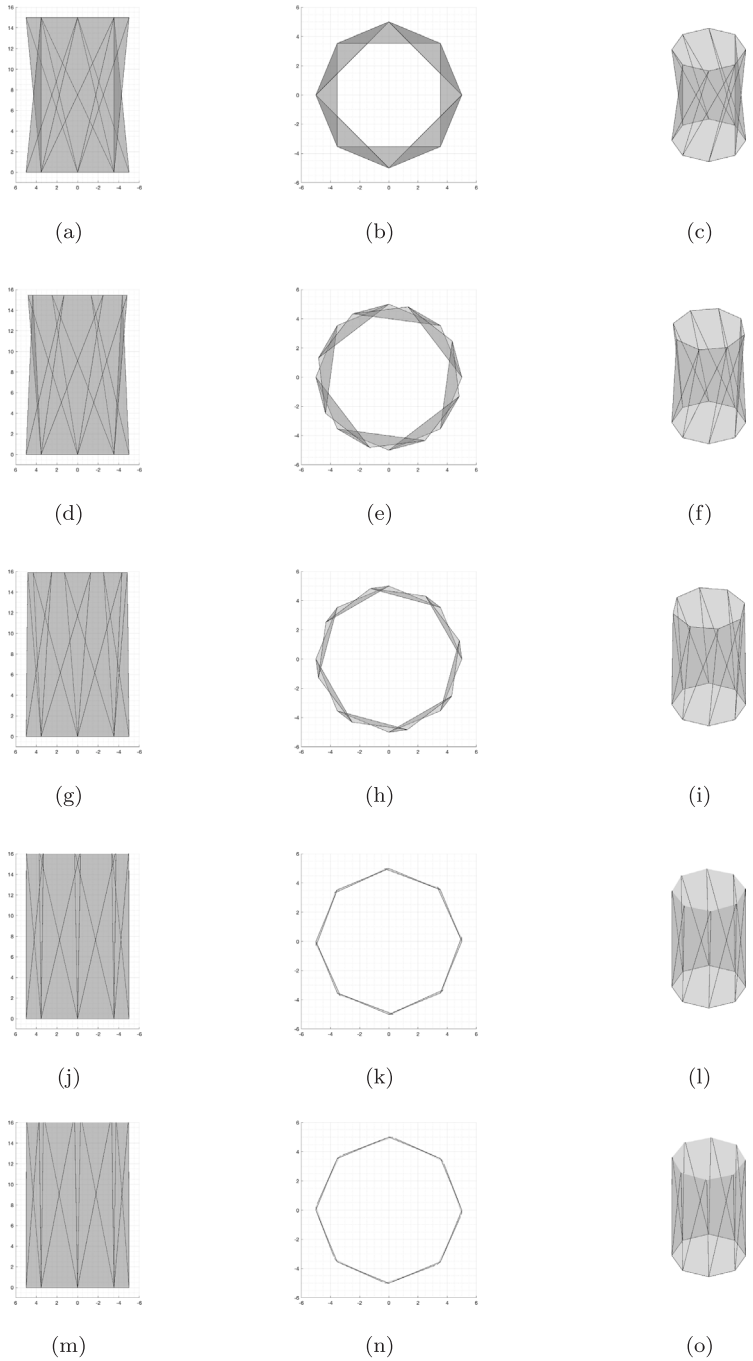

Fig. 8. Stroboscopic shoots for the lengthening test of the one-stage Kresling tube for $a/b = 1000$: side (on the left), top (on the middle) and 3D (on the right) views for $t/t_o = 0$ (first row), $t/t_o = 0.25$ (2nd row), $t/t_o = 0.5$ (3rd row), $t/t_o = 0.75$ (4th row) and $t/t_o = 1$ (5th row).

loading rate $\bar{v} = 1$ and considering as time-step length of the integration scheme $\Delta t = 0.001$, we perform a stepwise analysis for a time horizon $t_o = 1.8$.

Fig. 6, along with Figs. 7 and 8, give a synoptic view over the results of the performed numerical analysis.[7] These figures suggest that:

(1) in both considered cases the assigned (vertical) displacement time law induces a rotation of the nodes at the top base of the one-stage Kresling tube, see Figs. 6(a)–(d); the plots reporting $\vartheta(w)$, see Figs. 6(c)–(d), show a switch-like behavior characterized by rotation of the top base with high rate at the beginning and low rate in the second part of the test;

(2) looking at the plots of the energies, see Fig. 6(e)–(f), we observe a sharp jump of the strain energy associated to the folding, deriving from the introduction of an energy barrier avoiding the contact of adjacent facets, for the shortening test; furthermore, we observe that the stretching energy is higher than the folding energy, while the kinetic energy is practically negligible;

(3) the mechanical behavior observed in the numerical simulation aligns with that observed while playing with a one-stage Kresling tube made of paper board, see Figs. 7 and 8.

[7] In the supplementary materials we have also included the videoclips `K8x1shorteningaonb1000` and `K8x1lengtheningaonb1000` of the deformation of the tube subjected to, respectively, shortening and lengthening for $a/b = 1000$.

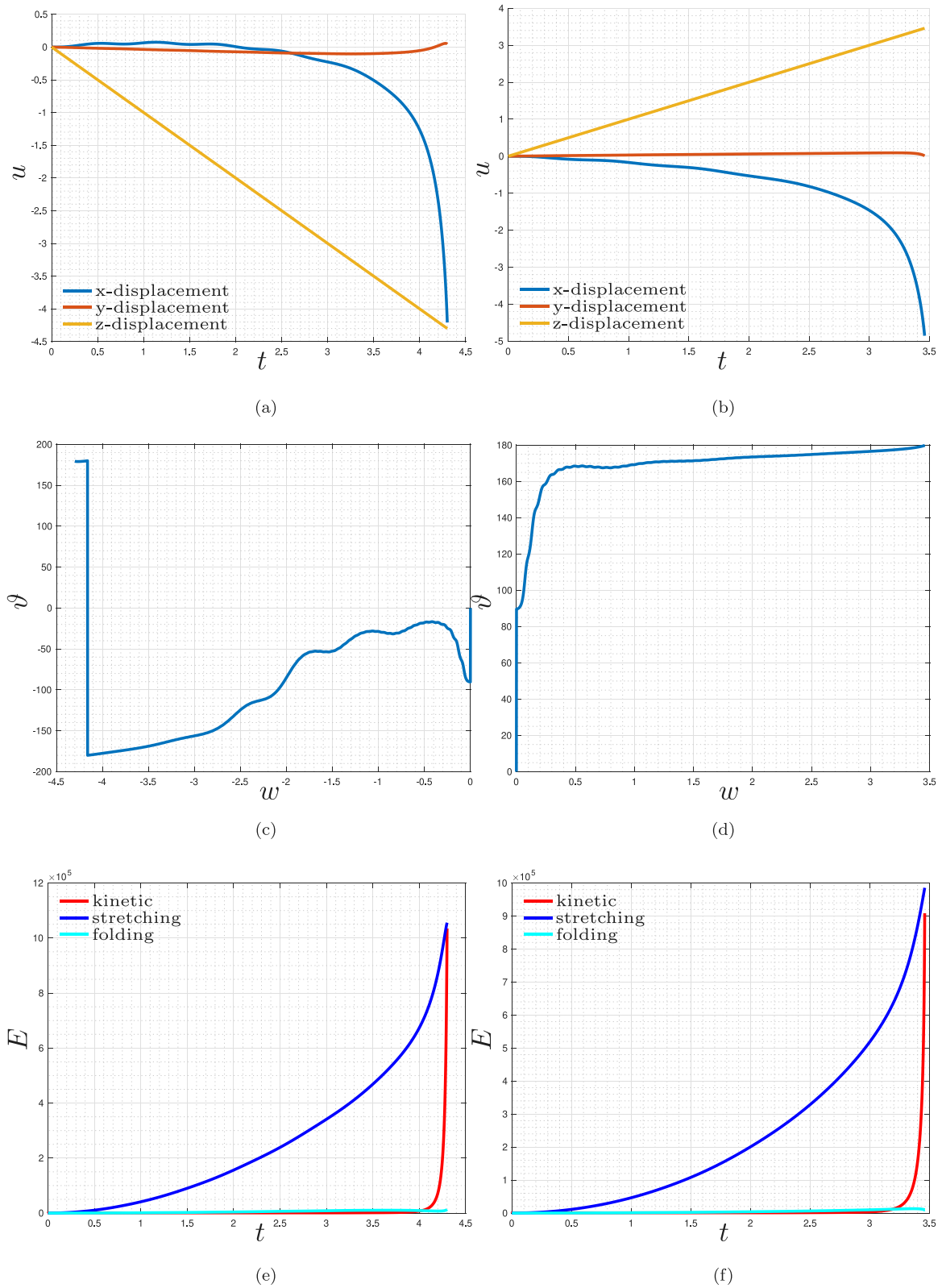

Fig. 9. Shortening (on the left) and lengthening (on the right) of the one-stage Kresling tube for $a/b = 0.1$: time evolution of the displacement of the 9th node (a), rotation of the tube's top base *vs.* assigned vertical displacement (b) and time evolution of energies – kinetic, stretching and folding – (c).

4.2. Shortening and lengthening tests for $a/b = 0.1$

We are here concerned with the second case study, namely shortening and lengthening tests of the Kresling tube metamaterial with stiffness ratio $a/b = 0.1$. We apply the same nodal conditions and, as before, we perform preliminarily a modal analysis in the reference configuration to compute the first T_1 and the last T_n natural periods needed to calibrate the parameters employed by the modified Casciaro's integration scheme. For this case, we have $T_1 = 2.87$ and $T_n = 0.0236$. Considering a loading velocity $\bar{v} = 1$, and considering again as time-

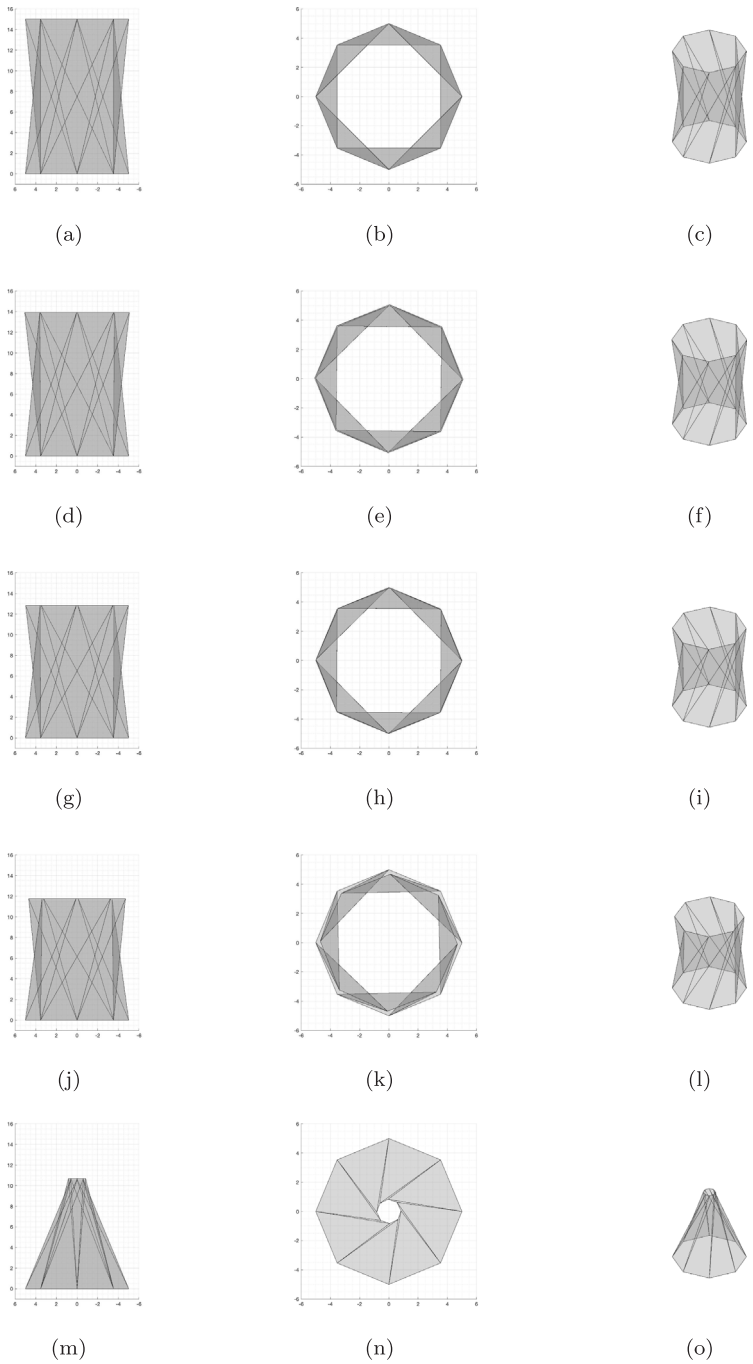

Fig. 10. Stroboscopic shoots for the shortening test of the one-stage Kresling tube for $a/b = 0.1$: side (on the left), top (on the middle) and 3D (on the right) views for $t/t_o = 0$ (first row), $t/t_o = 0.25$ (2nd row), $t/t_o = 0.5$ (3rd row), $t/t_o = 0.75$ (4th row) and $t/t_o = 1$ (5th row).

step length of the integration scheme $\Delta t = 0.001$, we perform stepwise analyses having time horizons equal to $t_o = 4.3$ and $t_o = 3.46$ for the shortening and lengthening test, respectively.

Also for this case study, the presented figures, namely Figs. 9–11 provide a synoptic overview of the results of the performed numerical experiments. From the presented plots – and also from the video-clips `K8x1shorteningaonb01` and `K8x1lengtheningaonb01` included in the supplementary materials – we deduce that:

(1) the assigned (vertical) displacement law induces a rotation of the nodes at the top base of the one-stage Kresling tube, see Figs. 9(a)–(d); the plots of $\vartheta(w)$ show also in this case the occurrence of a switch-like behavior characterized by rotation of the top base with high rate at the beginning and low rate in the second part of the tests, see Figs. 9(c)–(d);
(2) beside the rotation of the nodes at the top base of the one-stage Kresling tube, the buckling of the tube is characterized by shrinking of the top base, see Figs. 10 and 11;
(3) stretching energy is higher than folding energy, see Fig. 9(e)–(f); the shrinking of the top base also produces a sharp increment of the kinetic energy, see again Fig. 9(e)–(f);

It is at first worth to be remarked that both study cases, *i.e.* both analyzed stiffness ratios a/b, are characterized by strong nonlinearities, as large deformations and energy barriers are considered. Therefore, even the study case corresponding to a classical paperboard origami has exhibited behaviors that were not observed in previous studies, like the

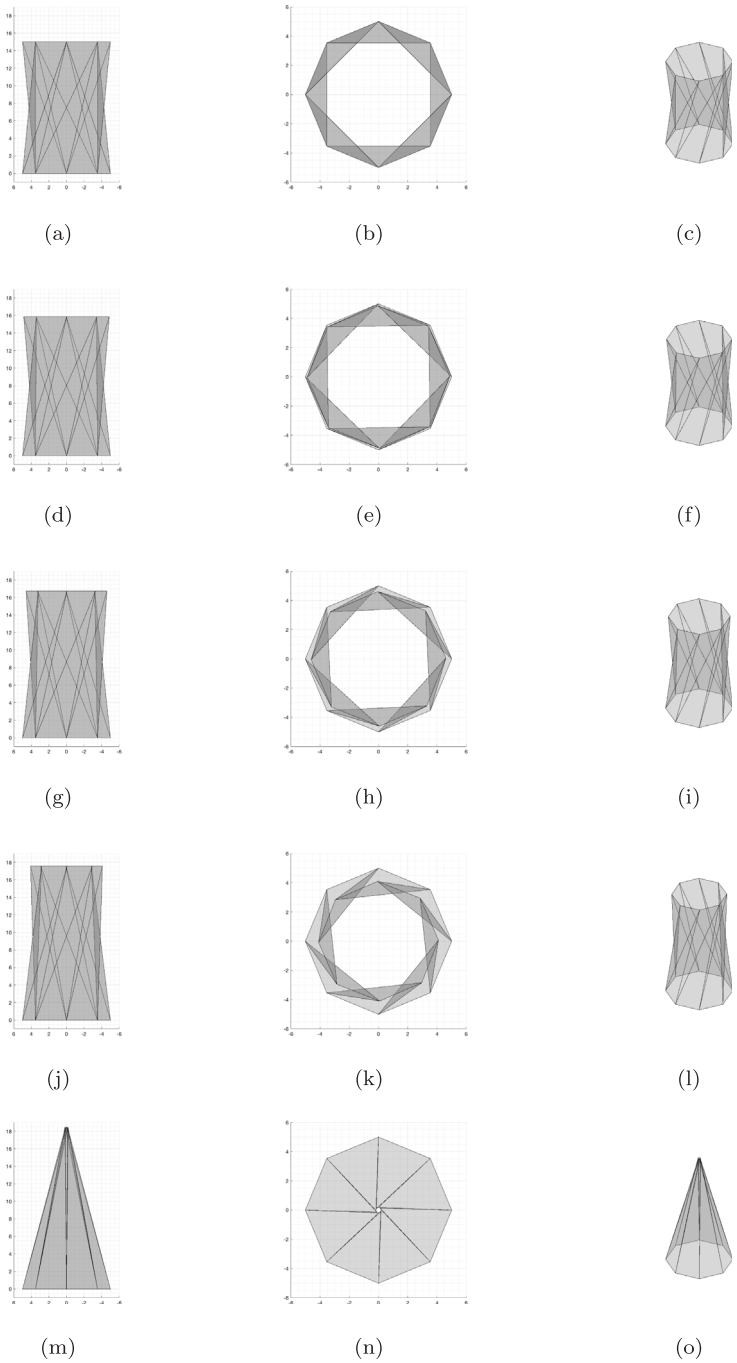

Fig. 11. Stroboscopic shoots for the lengthening test of the one-stage Kresling tube for $a/b = 0.1$: side (on the left), top (on the middle) and 3D (on the right) views for $t/t_o = 0$ (first row), $t/t_o = 0.25$ (2nd row), $t/t_o = 0.5$ (3rd row), $t/t_o = 0.75$ (4th row) and $t/t_o = 1$ (5th row).

buckling in (axial) extension. Additionally, when a low stiffness ratio a/b is considered, buckling occurs both in extension and compression and the main features of buckling seem to be unaffected by the loading direction, namely we have, besides its rotation, shrinking of the top base of the Kresling tube and an axial shortening of the tube for both the shortening and lengthening test. The aforementioned shrinking is due to the fact that a set of alternate facets are almost reaching a zero surface area. This is justified by the low relative cost, in terms of strain energy, of in-plane deformation of facets compared to folding of the origami around creases. The achievement of the exotic features conferred by a low stiffness ratio a/b, as that studied here, are in our opinion definitely worth the search for viable physical realizations of such a novel Kresling origami tube metamaterial.

5. Concluding remarks and future challenges

In this contribution we have presented the results of some numerical simulations concerning one-stage Kresling tube metamaterials subjected to shortening or lengthening in the tube axis direction. We proved that, for a fixed geometry, modifying the ratio between the stiffness parameter ruling the in-plane behavior and that ruling the folding one we obtain an unconventional dynamic buckling mode, triggered by a shortening, which produces a stenosis of the tube. Furthermore, we proved that such a stenosis is also produced if we consider a lengthening of the tube. This unexpected buckling behavior adds up to the several exotic buckling phenomena triggered by lengthening, see Eremeyev and Turco (2020), Zaccaria et al. (2011).

The numerical simulations described in the foregoing pave the way for studying a metamaterial which integrates the unconventional buckling of one-stage Kresling tubes.

Future developments and challenges include an in-depth study on possible real-world applications of the k-tube metamaterial, the optimization of the ratio a/b, see Desmorat et al. (2020), between in-plane and folding stiffnesses, the physical realization of k-tubes by means of 3D printing and the subsequent mechanical testing, the development of one/two-dimensional simplified continuum models, via homogenization processes, incorporating the coupling between shortening/lengthening and the consequent cross-sectional rotation (around the tube axis) and, possibly, stenosis. These phenomena should be taken into account in one-dimensional modeling through additional kinematic parameters. Kresling tube metamaterials constituted by several stages – *i.e.* storeys – and, possibly, proportionally many facets in a single stage, deserve to be explored from the mechanical point of view through the tools employed in the present work, since it is the expected that, when the ratio a/b is large, their behavior is caught by the so-called sine–Gordon equation, which possesses a solitary wave solution.

Regarding the physical realization of k-tubes by means of 3D printing, it would be interesting to attempt at designing extremely compliant microstructured facets, exploiting, as an instance, the pantographic motif. Facets might have a bi-pantographic (Barchiesi et al., 2020) microstructure. Furthermore, experimental campaigns could be focused on the assessment of different 3D-printing processes and raw materials in the manufacturing of k-tubes, in that they affect the mechanical and morphological properties of printed samples (De Angelo et al., 2019). To this end, the use of Digital Image Correlation (DIC) and Digital Volume Correlation (DVC) is envisaged, as they now constitute a consolidated tool to analyze kinematic details in experiments performed on metamaterials, a task that cannot be easily achieved by means of more classical measurement techniques like strain gauges or extensometers (Valmalle et al., 2023; Auger et al., 2020; Valmalle et al., 2022).

Finally, for the time being, we have assumed perfect adhesion among the facets. This could be not the case in presence of weak(ening) interfaces/sliding mechanisms among facets due to damage or on-purpose design. From the modeling point of view, points belonging to different facets and occupying the same position in space in the initial configuration would be allowed some relative kinematics. In the case of sliding mechanisms among adjacent facets, it would be required to use some internal kinematic constraint enforced through penalization, a proper non-constrained reduced kinematics, or Lagrange multipliers. In the case of elastic elements opposing to relative movements among adjacent facets, an energy term would be required. From the continuum point of view, the utilization of a mixture theory employing several displacement fields, see Placidi and Hutter (2006), would probably be required. In that case, some directional displacement derivatives would be constrained or penalized in the strain energy, respectively. Future attempts at considering these situations should be based on existing contributions (Spagnuolo et al., 2017).

CRediT authorship contribution statement

Emilio Turco: Writing – review & editing, Writing – original draft, Visualization, Validation, Supervision, Software, Resources, Project administration, Methodology, Investigation, Funding acquisition, Formal analysis, Data curation, Conceptualization. **Emilio Barchiesi:** Writing – review & editing, Writing – original draft, Visualization, Validation, Supervision, Software, Resources, Project administration, Methodology, Investigation, Funding acquisition, Formal analysis, Data curation, Conceptualization. **Andrea Causin:** Writing – review & editing, Writing – original draft, Visualization, Validation, Supervision, Software, Resources, Project administration, Methodology, Investigation, Funding acquisition, Formal analysis, Data curation, Conceptualization. **Francesco dell'Isola:** Writing – review & editing, Writing – original draft, Visualization, Validation, Supervision, Software, Resources, Project administration, Methodology, Investigation, Funding acquisition, Formal analysis, Data curation, Conceptualization. **Margherita Solci:** Writing – review & editing, Writing – original draft, Visualization, Validation, Supervision, Software, Resources, Project administration, Methodology, Investigation, Funding acquisition, Formal analysis, Data curation, Conceptualization.

Declaration of competing interest

The authors declare that they have no known competing financial interests or personal relationships that could have appeared to influence the work reported in this paper.

Data availability

No data was used for the research described in the article.

Acknowledgments

Emilio Turco, Andrea Causin and Margherita Solci gratefully acknowledge the support of the University of Sassari, Italy (Fondo di Ateneo per la ricerca 2020).

Appendix A. Supplementary data

Supplementary material related to this article can be found online at https://doi.org/10.1016/j.ijsolstr.2024.112925.

References

Abel, J.F., Cooke, J.R. (Eds.), 2008. Deployable structures and biological morphology. In: Proceedings of the 6th International Conference on Computation of Shell and Spatial Structures.

Abali, B.E., Müller, W.H., Eremeyev, V.A., 2015. Strain gradient elasticity with geometric nonlinearities and its computational evaluation. Mech. Adv. Mater. Modern Process. 1 (4), 1–11.

Abdoul-Anziz, H., Seppecher, P., 2018. Homogenization of periodic graph-based elastic structures. J. Ecole Polytech. – Math. 5, 259–288.

Al-Mansoori, M., Khan, K.A., Cantwell, W.J., 2020. Harnessing architected stiffeners to manufacture origami-inspired foldable composite structures. Compos. Sci. Technol. 200 (108449), 1–11.

Alibert, J.-J., Seppecher, P., dell'Isola, F., 2003. Truss modular beams with deformation energy depending on higher displacement gradients. Math. Mech. Solids 8 (1), 51–73.

Altenbach, H., Eremeyev, V.A., 2009. Shell structures: Theory and applications (volume 2). In: Chapter on the Shell and Plate Theories with Surface Stresses. Taylor & Francis Group.

Altenbach, H., Eremeyev, V.A., 2013. Large deformations of inelastic shells. Key Eng. Mater. 535, 76–79.

Andreaus, U., Spagnuolo, M., Lekszycki, T., Eugster, S.R., 2018. A ritz approach for the static analysis of planar pantographic structures modeled with nonlinear Euler–Bernoulli beams. Contin. Mech. Thermodyn. 30, 1103–1123.

Argyris, J., Tenek, L., Olofsson, L., 1997. TRIC: a simple but sophisticated 3-node triangular element based on 6 rigid-body and 12 straining modes for fast computational simulations of arbitrary isotropic and laminated composite shells. Comput. Methods Appl. Mech. Engrg. 145, 11–85.

Aristodemo, M., 1985. A high-continuity finite element model for two-dimensional elastic problems. Comput. Struct. 21 (5), 987–993.

Auger, P., Lavigne, T., Smaniotto, B., Spagnuolo, M., dell'Isola, F., Hild, F., 2020. Poynting effects in pantographic metamaterial captured via multiscale DVC. J. Strain Anal. Eng. Des. http://dx.doi.org/10.1177/0309324720976625.

Balobanov, V., Khakalo, S., Niiranen, J., 2019. Strain gradient elasticity in structural mechanics: Isogeometric implementations and applications to microarchitectured materials. In: 5th ECCOMAS Young Investigators Conference, YIC 2019. pp. 337–339.

Barchiesi, E., dell'Isola, F., Hild, F., Seppecher, P., 2020. Two-dimensional continua capable of large elastic extension in two independent directions: Asymptotic homogenization, numerical simulations and experimental evidence. Mech. Res. Commun. 103, 103466.

Barchiesi, E., Spagnuolo, M., Placidi, L., 2019. Mechanical metamaterials: a state of the art. Math. Mech. Solids 24 (1), 212–234.

Baroudi, D., Giorgio, I., Battista, A., Turco, E., Igumnov, L.I., 2019. Nonlinear dynamics of uniformly loaded elastica: Experimental and numerical evidence of motion around curled stable equilibrium configurations. ZAMM Z. Angew. Math. Mech. 99 (7), 1–20.

Casciaro, R., 1975. Time evolutional analysis of nonlinear structures. Meccanica 3 (X), 156–167.

Cazzani, A., Malagù, M., Turco, E., 2016a. Isogeometric analysis of plane curved beams. Math. Mech. Solids 21 (5), 562–577.

Cazzani, A., Malagù, M., Turco, E., Stochino, F., 2016b. Constitutive models for strongly curved beams in the frame of isogeometric analysis. Math. Mech. Solids 21 (2), 182–209.

Chang, Z., Tu, T.D., Narumi, K., Kim, H., 2020. Kirigami haptic swatches: Design methods for cut-and-fold haptic feedback mechanisms. In: CHI 2020, no. 526. Association for Computing Machinery, Honolulu, HI, USA, pp. 1–12.

Chong, K., Pertigkiozoglou, E., Saad, C., Stack, A., 2017. 8Twist, fall.

Cosserat, E., Cosserat, F., 1896. Sur la théorie de l'élasticité. Premier mémoire. In: Annales de la Faculté des sciences de Toulouse: Mathématiques, Vol. 10. pp. I1–I116.

De Angelo, M., Spagnuolo, M., D'annibale, F., Pfaff, A., Hoschke, Klaus, Misra, Aviral, Dupuy, Corinne, Peyre, Patrice, Dirrenberger, J., Pawlikowski, M., 2019. The macroscopic behavior of pantographic sheets depends mainly on their microstructure: experimental evidence and qualitative analysis of damage in metallic specimens. Contin. Mech. Thermodyn. 31, 1181–1203.

dell'Isola, F., Andreaus, U., Placidi, L., 2015. At the origins and in the vanguard of peridynamics, non-local and higher-gradient continuum mechanics: An underestimated and still topical contribution of gabrio piola. Math. Mech. Solids 20 (8), 887–928.

dell'Isola, F., Giorgio, I., Pawlikowski, M., Rizzi, N.L., 2016. Large deformations of planar extensible beams and pantographic lattices: Heuristic homogenisation, experimental and numerical examples of equilibrium. Proc. R. Soc. London A 472 (2185), 1–23.

dell'Isola, F., Seppecher, P., Spagnuolo, M., Barchiesi, E., Hild, F., Lekszycki, T., Giorgio, I., Placidi, L., Andreaus, U., Cuomo, M., Eugster, S.R., Pfaff, A., Hoschke, K., Langkemper, R., Turco, E., Sarikaya, R., Misra, A., De Angelo, M., D'Annibale, F., Bouterf, A., Pinelli, X., Misra, A., Desmorat, B., Pawlikowski, M., Dupuy, C., Scerrato, D., Peyre, P., Laudato, M., Manzari, L., Göransson, P., Hesch, C., Hesch, S., Franciosi, P., Dirrenberger, J., Maurin, F., Vangelatos, Z., Grigoropoulos, C., Melissinaki, V., Farsari, M., Muller, W., Emek Abali, B., Liebold, C., Ganzosch, G., Harrison, P., Drobnicki, R., Igumnov, L., Alzahrani, F., Hayat, T., 2019. Advances in pantographic structures: design, manufacturing, models, experiments and image analyses. Contin. Mech. Thermodyn. 31 (4), 1231–1282.

Desmorat, B., Spagnuolo, M., Turco, E., 2020. Stiffness optimization in nonlinear pantographic structures. Math. Mech. Solids 25 (11), 2252–2262.

Eremeyev, V.A., Aifantis, E.C., 2017. On extended models of plates based on linear strain gradient elasticity. In: Shell Structures: Theory and Applications, Vol. 4. CRC Press, pp. 85–88.

Eremeyev, V.A., Turco, E., 2020. Enriched buckling for beam-lattice metamaterials. Mech. Res. Commun. 103 (103458), 1–7.

Forte, A.E., Melancon, D., Zanati, M., De Giorgi, M., Bertoldi, K., 2023. Chiral mechanical metamaterials for tunable optical transmittance. Adv. Funct. Mater. 33 (20), 2214897, (1–7).

Georgakopolous, S., Tentzeris, E., Cook, B., 2015. Origami folded antennas. United States Patent n. US 9 214, 722 B2, December, 15.

Greco, L., Cuomo, M., 2013. B-spline interpolation of Kirchhoff–Love space rods. Comput. Methods Appl. Mech. Engrg. 256, 251–269.

Green, A.E., Naghdi, P.M., Wainwright, W.L., 1965. A general theory of a cosserat surface. Arch. Ration. Mech. Anal. 20, 287–308.

Hencky, H., 1921. "Uber die angenäherte Lösung von Stabilitätsproblemen im Raum mittels der elastischen Gelenkkette (Ph.D. thesis). Engelmann.

Hunt, G.W., Ario, I., 2005. Twist buckling and the foldable cylinder: an exercise in origami. Int. J. Non-Linear Mech. 40, 833–843.

Kadic, M., Milton, G.W., van Hecke, M., Wagener, M., 2019. 3D metamaterials. Nat. Rev. Phys. 1, 198–210.

Kamrava, S., Mousanezhad, D., Ebrahimi, H., Ghosh, R., Vaziri, A., 2017. Origami-based cellular metamaterial with auxetic, bistable, and self-locking properties. Sci. Rep. 7 (46046), 1–9.

Kaufmann, J., Bhovad, P., Li, S., 2021. Harnessing the multistability of Kresling origami for reconfigurable articulation in soft robotic arms. Soft Robot. (2020), 1–12. http://dx.doi.org/10.1089/soro.0075.

Khakalo, S., Niiranen, J., 2017. Isogeometric analysis of higher-order gradient elasticity by user elements of a commercial finite element software. Comput. Aided Des. 82, 154–169.

Kim, Y., Cha, Y., 2020. Soft pneumatic gripper with a tendon-driven soft origami pump. Front. Bioeng. Biotechnol. 8.

Kresling, B., 1994. Hommage à Miura. Symmetry: Culture Sci. 5 (1), 23–36.

Kuribayashi, K., Tsuchiya, K., You, Z., Tomus, D., Umemoto, M., Ita, T., Sasaki, M., 2006. Self-deployable origami stent grafts as a biomedical application of Ni-rich TiNi shape memory alloy foil. Mater. Sci. Eng. A 419, 131–137.

Liu, K., Paulino, G.H., 2017. Nonlinear mechanics of non-rigid origami: an efficient computational approach. Proc. R. Soc. A.

Liu, K., Tachi, T., Paulino, G.H., 2021. Bio-inspired origami metamaterials with metastable phases through mechanical phase transitions. J. Appl. Mech. ASME 88 (091002), 1–10.

Masana, R., Khazaaleh, S., Alhussein, H., Crespo, R.S., Daqaq, M.F., 2020. An origami-inspired dynamically actuated binary switch. Appl. Phys. Lett. 117 (081901).

Maugin, G.A., 2013. Continuum mechanics through the twentieth century. In: Solid Mechanics and Its Applications, vol. 196, Springer.

Milton, G.W., Cherkaev, A.V., 1995. Which elasticity tensors are realizable? J. Eng. Mater. Technol. 117 (4), 483–493.

Mindlin, R.D., 1965. Second gradient of strain and surface-tension in linear elasticity. Int. J. Solids Struct. 1 (4), 417–438.

Miura, K., 1985. Method of Packaging and Deployment of Large Membranes in Space. Report 618, The Institute of Space and Astronautical Science.

Niiranen, J., Khakalo, S., Balobanov, V., Kiendl, J., Niemi, A.H., Hosseini, B., Reali, A., 2016. Isogeometric Galerkin methods for gradient-elastic bars, beams, membranes and plates. In: Papadrakis, M., Papadopoulos, V., Stefanou, G., Plevris, V. (Eds.), ECCOMAS Congress 2016. Crete Island, Greece, pp. 5–10.

Placidi, L., Hutter, K., 2006. Thermodynamics of polycrystalline materials treated by the theory of mixtures with continuous diversity. Contin. Mech. Thermodyn. 17, 409–451.

Spagnuolo, M., Andreaus, U., 2018. A targeted review on large deformations of planar elastic beams: extensibility, distributed loads, buckling and post-buckling. Math. Mech. Solids 108128651773700.

Spagnuolo, M., Barcz, K., Pfaff, A., dell'Isola, F., Franciosi, P., 2017. Qualitative pivot damage analysis in aluminum printed pantographic sheets: Numerics and experiments. Mech. Res. Commun. 83, 47–52.

Steigmann, D.J., Faulkner, M.G., 1993. Variational theory for spatial rods. J. Elasticity 33 (1), 1–26.

Toupin, R.A., 1964. Theories of elasticity with couple-stress. Arch. Ration. Mech. Anal. 17 (2), 85–112.

Tran, C.A., Barchiesi, E., 2022. A new block-based approach for the analysis of damage in masonries undergoing large deformations. Contin. Mech. Thermodyn. 1–30. http://dx.doi.org/10.1007/s00161-022-01178-5.

Tran, C.A., Barchiesi, E., Placidi, L., León Trujillo, F.J., 2021. A block-based variational elasto-damage model for masonry analysis inspired from granular micromechanics: Preliminary study. Mech. Res. Commun. 118 (103802), 1–6.

Turco, E., 2018a. Discrete is it enough? The revival of Piola–Hencky keynotes to analyze three-dimensional elastica. Contin. Mech. Thermodyn. 30 (5), 1039–1057.

Turco, E., 2018b. In-plane shear loading of granular membranes modeled as a Lagrangian assembly of rotating elastic particles. Mech. Res. Commun. 92, 61–66.

Turco, E., 2021. Stepwise analysis of pantographic beams subjected to impulsive loads. Math. Mech. Solids 26 (1), 62–79.

Turco, E., 2022. Forecasting nonlinear vibrations of patches of granular materials by elastic interactions between spheres. Mech. Res. Commun. 122 (103879), 1–5.

Turco, E., Barchiesi, E., Causin, A., dell'Isola, F., Solci, M., 2023a. Kresling tube metamaterial exhibits extreme large-displacement buckling behavior. Mech. Res. Commun. 134 (104202), 1–7.

Turco, E., Barchiesi, E., dell'Isola, F., 2022. In-plane dynamic buckling of duoskelion beam-like structures: discrete modeling and numerical results. Math. Mech. Solids 27 (7), 1164–1184.

Turco, E., Barchiesi, E., dell'Isola, F., 2023b. Nonlinear dynamics of origami metamaterials: energetic discrete approach accounting for bending and in-plane deformation of facets. Z. Angew. Math. Phys. 74 (26), 1–29.

Turco, E., dell'Isola, F., Cazzani, A., Rizzi, N.L., 2016a. Hencky-type discrete model for pantographic structures: numerical comparison with second gradient continuum models. Z. Angew. Math. Phys. 67 (85), 1–28.

Turco, E., dell'Isola, F., Misra, A., 2019. A nonlinear Lagrangian particle model for grains assemblies including grain relative rotations. Int. J. Numer. Anal. Methods Geomech. 43 (5), 1051–1079.

Turco, E., dell'Isola, F., Rizzi, N.L., Grygoruk, R., Müller, W.H., Liebold, C., 2016b. Fiber rupture in sheared planar pantographic sheets: numerical and experimental evidence. Mech. Res. Commun. 76, 86–90.

Turco, E., Golaszewski, M., Cazzani, A., Rizzi, N.L., 2016c. Large deformations induced in planar pantographic sheets by loads applied on fibers: experimental validation of a discrete Lagrangian model. Mech. Res. Commun. 76, 51–56.

Turco, E., Golaszewski, M., Giorgio, I., D'Annibale, F., 2017. Pantographic lattices with non-orthogonal fibres: experiments and their numerical simulations. Composites B 118, 1–14.

Turco, E., Misra, A., Pawlikowski, M., dell'Isola, F., Hild, F., 2018. Enhanced Piola–Hencky discrete models for pantographic sheets with pivots without deformation energy: numerics and experiments. Int. J. Solids Struct. 147, 94–109.

Turco, E., Rizzi, N.L., 2016. Pantographic structures presenting statistically distributed defects: numerical investigations of the effects on deformation fields. Mech. Res. Commun. 77, 65–69.

Valmalle, M., Smaniotto, B., Spagnuolo, M., Ciallella, A., Hild, F., 2023. Mesoscale DVC analyses and parameter calibration for pantographic block in 3-point flexure. Eur. J. Mech. A Solids 101 (105063), 1–14.

Valmalle, M., Vintache, A., Smaniotto, B., Gutmann, F., Spagnuolo, M., Ciallella, A., Hild, F., 2022. Local–global DVC analyses confirm theoretical predictions for deformation and damage onset in torsion of pantographic metamaterial. Mech. Mater. 172 (104379), 1–16.

Vincent, J.F.V., 2000. Deployable structures in nature: potential for biomimicking. Proc. Inst. Mech. Eng. C 214 (1), 1–10.

Wheatcroft, E.D., Shen, J., Groh, R.M.J., Pirrera, A., Schenk, M., 2023. Structural function from sequential, interacting elastic instabilities. Proc. R. Soc. London A 2022, 1–20. http://dx.doi.org/10.1098/rspa.0861.

Yasuda, H., Miyazawa, Y., Charalampidis, E.G., Chong, C., Kevrekidis, P.G., Yang, J., 2019. Origami-based impact mitigation via rarefaction solitary wave creation. Sci. Adv. 5 (5), 1–8.

Zaccaria, D., Bigoni, D., Noselli, G., Misseroni, D., 2011. Structures buckling under tensile dead load. Proc. R. Soc. A 467 (2130), 1686–1700.

Ze, Q., Wu, S., Nishikawa, J., Dai, J., Sun, Y., Leanza, S., Zemelka, C., Novelino, L.S., Paulino, G.H., Zhao, R.R., 2022. Soft robotic origami crawler. Sci. Adv. 8 (eabm7834), 1–9.